ADVANCED MATERIALS
www.advmat.de

Preintercalation Strategy in Manganese Oxides for Electrochemical Energy Storage: Review and Prospects

*Qinghe Zhao, Aoye Song, Shouxiang Ding, Runzhi Qin, Yanhui Cui, Shuning Li, and Feng Pan**

Manganese oxides (MnO_2) are promising cathode materials for various kinds of battery applications, including Li-ion, Na-ion, Mg-ion, and Zn-ion batteries, etc., due to their low-cost and high-capacity. However, the practical application of MnO_2 cathodes has been restricted by some critical issues including low electronic conductivity, low utilization of discharge depth, sluggish diffusion kinetics, and structural instability upon cycling. Preintercalation of ions/molecules into the crystal structure with/without structural reconstruction provides essential optimizations to alleviate these issues. Here, the intrinsic advantages and mechanisms of the preintercalation strategy in enhancing electronic conductivity, activating more active sites, promoting diffusion kinetics, and stabilizing the structural integrity of MnO_2 cathode materials are summarized. The current challenges related to the preintercalation strategy, along with prospects for the future research and development regarding its implementation in the design of high-performance MnO_2 cathodes for the next-generation batteries are also discussed.

1. Introduction

Nowadays, the renewable energy sources, such as solar, wind, etc., have become worldwide hotspots, which call for the research and development of high-efficiency energy storage/conversion devices.[1–4] Up to now, the rechargeable batteries and supercapacitors have been considered as the most promising candidates for energy storage/conversion in electronic vehicles, portable devices, as well as large-scale energy storage devices,[5–8] which convert the chemical energy into electronic energy via shuttling ions between the cathodes and the anodes. Due to the low-cost, high-capacity, and environmentally friendliness, MnO_2-based materials have long been investigated as cathode materials in different kinds of batteries, including alkaline Zn/MnO_2 batteries,[9] Li-ion,[10,11] Na-ion,[12] Mg-ion,[13,14] and Zn-ion batteries.[15–17] Besides, MnO_2 is also one of the most suitable electrode material candidates due to its high theoretical pseudocapacitance (≈1370 F g^{-1}).[18] Despite these advancements over the past decades, some issues of MnO_2-based cathodes still remain due to the low electronic conductivity,[19–21] low utilization of reversible discharge depth,[22,23] sluggish diffusion kinetics,[24–26] and poor structural stability upon cycling,[27–29] which restricts their practical application in the commercial secondary batteries. Taking the Zn-ion batteries as example, the MnO_2 cathode seriously suffer from the above issues, especially the sluggish Zn^{2+} diffusion,[30] and structural collapse issue during H^+/Zn^{2+} intercalation/ extraction cycles.[31–33] Regarding these bottlenecks, researchers have strived to develop strategies that can realize optimizations in capacity, rate, and cycling properties of MnO_2 cathodes, such as surface coating,[34] metal-doping,[35] preintercalation,[36] etc. Among all the strategies, preintercalation strategy provides a basic and effective method for optimizing the structure and electrochemical performance of MnO_2-based cathodes.

In recent years, the preintercalation strategy has attracted much attention as an effective approach to enhance the electrochemical performance of cathode materials, including vanadate,[37] manganese oxides,[23] layered $LiCoO_2$,[38] etc. Several reviews and prospects have been conducted for MnO_2 materials. Some reviews have mentioned the electrochemical properties and correlated reaction mechanism of MnO_2 materials in aqueous Zn batteries,[29,39,40] and a review by Mai's group offers insights into the rational design of preintercalation electrodes in next-generation rechargeable batteries.[36] However, a review or prospect on the application and mechanism of the preintercalation strategy in MnO_2 materials for next-generation batteries is lacking. For MnO_2 electrode materials, many reports on improving the electrochemical properties of materials by applying preintercalation strategy have been emerged in the last 5 years (Table S1 in the Supporting Information). The main feature of the preintercalated MnO_2 materials is that some ions/molecules are preintercalated into the tunnel or interlayer hosts of MnO_2 materials prior to the battery cycling (or during synthesis process). These intercalated guest species, including ions, inorganic/organic molecules, as well as polymers, present electrostatic and physical interactions with the host framework and the inserted carrier ions via chemical bonding or coordination, presenting significant benefiting effect on the inherent structure of hosts and the transport kinetics of carrier ions. Generally, there are several

Dr. Q. Zhao, A. Song, S. Ding, Dr. R. Qin, Dr. Y. Cui, Dr. S. Li, Prof. F. Pan
School of Advanced Materials
Peking University
Shenzhen Graduate School
Shenzhen 518055, China
E-mail: panfeng@pkusz.edu.cn

The ORCID identification number(s) for the author(s) of this article can be found under https://doi.org/10.1002/adma.202002450.

DOI: 10.1002/adma.202002450

approaches to achieve the preintercalated MnO_2-based materials, including hydrothermal synthesis,[41,42] calcination treatment,[43] ion-exchange reaction,[44,45] aqueous/organic interfacial synthesis,[24,46] electrochemical reactions,[47] and so on. Given the above different synthesis reactions, the obtained preintercalated MnO_2 are different, and the details of each approaches will be described in the later section. During charge/discharge cycles, the corresponding electrochemical reaction of carrier ions (C^{n+}) in preintercalated MnO_2 ($AMnO_2$) electrodes is as follows

$$C_xAMnO_2 \rightleftarrows AMnO_2 + xC^{n+} + xne^- \quad (1)$$

where C^{n+} ($n = 1, 2, 3$) represents the carrier ions, and A represents the preintercalated ions/ molecules.

To clarify the benefiting effect of preintercalation strategy, a series of concrete examples are given as below. The poor rate performance of MnO_2 materials has long been an obstacle for their intrinsically low electronic conductivity. To overcome this obstacle, Yuan et al.[22] proposed that the preintercalated K^+ ions inside 2×2 tunnels of α-MnO_2 can increase the electronic conductivity, and improve Li^+ diffusivity. The MnO_2 materials also suffer from the sluggish diffusion kinetics for various kinds of carrier ions, especially for diffusion of multivalent ions, such as Zn^{2+}, Mg^{2+}, etc. Kang et al.[48] suggested that the activation barrier for Li^+ hopping in layered lithium transition metal oxides is strongly affected by the value of interlayer spacing and electrostatic interactions between inserted Li^+ ions and host anions. Thus, expanding interlayer spacing[49,50] and decreasing electrostatic interactions between carrier ions and host anions via "charge shielding" effect of crystal water[51,52] has been reported in many literatures to promote the diffusion kinetics of carrier ions in MnO_2 cathodes for various battery applications. The tunnel/layer structure of MnO_2 materials will be highly distorted or destructed during cycling, leading to Mn^{2+} dissolution, formation of the inactive spinel-type materials,[53,54] and eventually cause capacity fading. Preintercalation can greatly reduce these capacity fading issues induced by structural instability upon cycling, due to the reduced volumetric variation during insertion/extraction process of the carrier ions. For instance, the polyaniline preintercalated δ-MnO_2,[24] the 3D M_xMnO_2 (M = Li, Na, K, Co, and Mg),[26] the alkali ion intercalated compounds A–M–O(A = Li, Na, K, Rb; M = V, Mo, Co, Mn),[38] the TMA^+ stabilized δ-MnO_2,[45] and K^+ intercalated MnO_2[55] have been utilized as cathodes to obtain long-life reversible Li-ion, Na-ion, K-ion, Mg-ion, and Zn-ion batteries, respectively.

The previous reports have illustrated that the preintercalation strategy in MnO_2 cathodes benefit for the extended cycling performance, outstanding rate properties, as well as higher reversible capacity. However, despite these reports, the overall mechanisms explaining how the preintercalation strategy enhance the battery performance of MnO_2 cathodes are still ambiguous. Herein, we summarize all the previously reported preintercalation approaches, compare electrochemical performance of the preintercalated MnO_2 cathodes versus the corresponding pristine cathodes, and reveal the intrinsic mechanisms of preintercalation on enhancing electronic conductivity, activating more active sites, promoting diffusion kinetics, and stabilizing structure integrity of MnO_2 cathodes to affect the corresponding electrochemical performance. Finally, we also make prospects on future research and development for designing high-performance MnO_2 cathodes based on the preintercalation strategy for the next-generation batteries.

2. Synthesis Approaches for Preintercalated MnO_2 Materials

As discussed above, we first introduce some normal synthesis approaches to obtain the preintercalated MnO_2 materials. There are several typical preintercalation approaches for MnO_2-based materials,[56] including hydrothermal synthesis, calcination treatment, ion-exchange reaction, aqueous/organic interfacial reactions, electrodeposition, and so on. The hydrothermal synthesis is the most common method for synthesis of preintercalated MnO_2. Chen et al.[57] reported that the Ce^{3+} intercalated α-MnO_2 was synthesized using a simple hydrothermal reaction in a solution containing Ce^{3+} ions. As a pseudocapacitive electrode material, this Ce^{3+} intercalated α-MnO_2 presented 10-fold higher specific capacitance compared with that of the pristine MnO_2. Lin et al.[55] developed a facile "hydrothermal potassiation" strategy, which could effectively increase the intercalated K^+ content in birnessite. First, the precursor $K_{0.18}MnO_2{\cdot}0.51H_2O$ was grown on the carbon cloth collector by hydrothermal reaction at a low temperature of 120 °C. Subsequently, the "hydrothermal potassiation" step in KOH solution was conducted in a higher temperature of 205 °C, and thus samples with various intercalated K contents and crystal water could be obtained (**Figure 1**a), as shown in the reaction in Equation (2)

$$K_{0.18}MnO_2{\cdot}0.61H_2O + xK_2SO_4 \rightarrow K_{0.18+x}MnO_2{\cdot}yH_2O + (0.61-y)H_2O + xH_2SO_4 + 0.5xO_2 \quad (2)$$

where the x value varies with different hydrothermal times. The abovementioned hydrothermal methods are very simple, efficient, and suitable for large-scale synthesis, however, it is difficult to use this method to synthesize δ-MnO_2 materials with larger interlayer spacing (e.g., $d_{001} > 8$ Å).

Calcination treatment can also be a feasible method for synthesis of the preintercalated MnO_2 materials. Wang et al.[50] synthesized a novel K^+-intercalated layered Fe/Mn-based oxide material ($K_{0.7}Fe_{0.5}Mn_{0.5}O_2$) using the calcination treatment at high temperature of 500–1000 °C (Figure 1b). The as-prepared $K_{0.7}Fe_{0.5}Mn_{0.5}O_2$ displayed both higher capacity and superior cycling stability as a cathode for Na-ion batteries. The intercalated K^+ not only acts as interlayer pillars to protect the layered structure from collapse, but also expands the interlayer structure to achieve the increased Na^+ diffusion coefficient. The calcination treatment is advantageous to achieve perfect crystal structure and enhance the structural stability of MnO_2-based materials. The above hydrothermal and calcination reaction is as the the reaction in Equation (3)

$$0.7KNO_3 + 0.5Fe(NO_3)_3 + 0.5Mn(NO_3)_2 + H_2C_2O_4 + 0.32H_2O \rightarrow K_{0.7}Fe_{0.5}Mn_{0.5}O_2 + 2CO_2 + 0.28N_2 + 2.64HNO_3 \quad (3)$$

However, the calcination treatment completely removes the crystal water, making it very difficult for the insertion/extraction

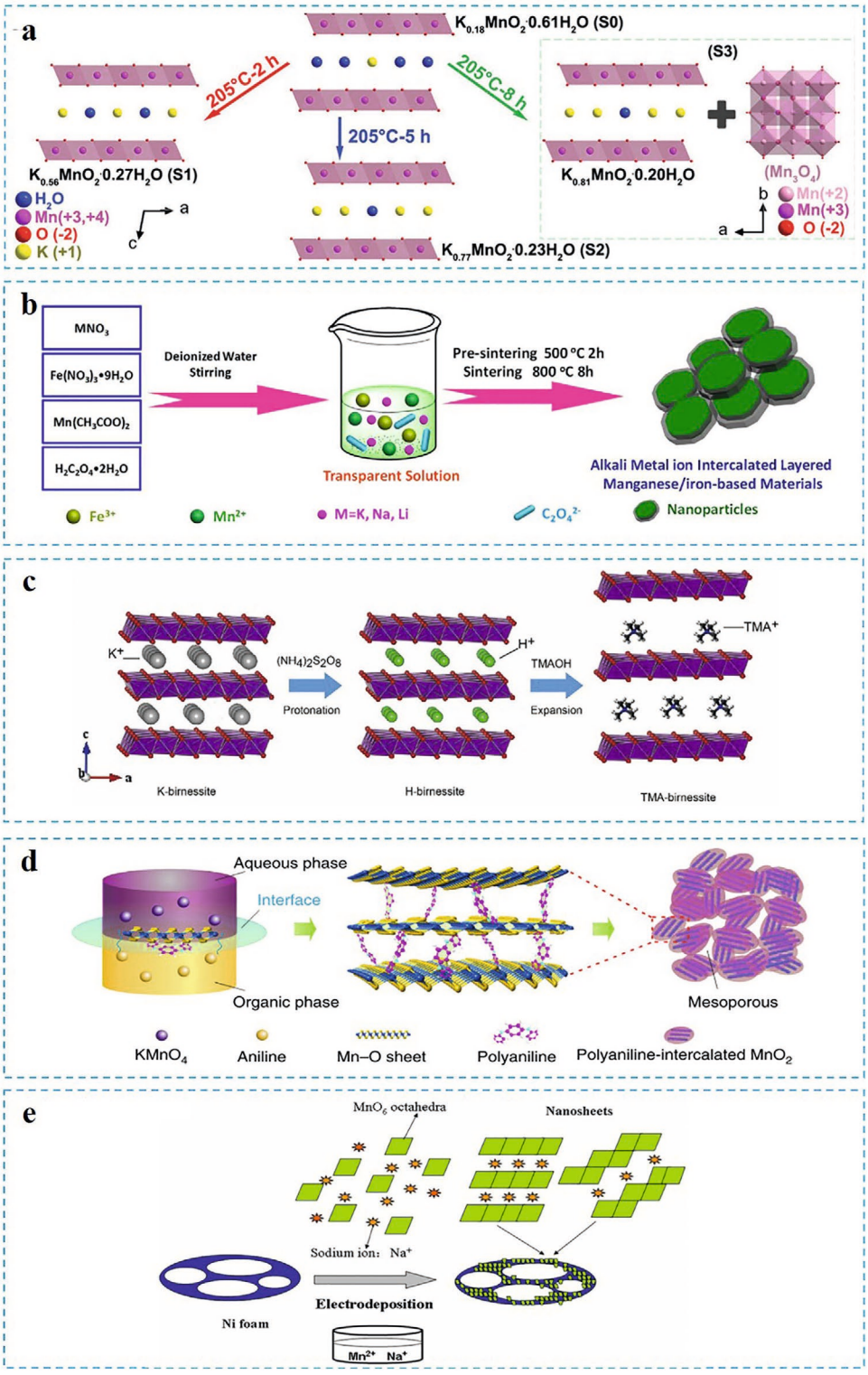

Figure 1. Various synthesis approaches of preintercalated MnO_2 materials. a) Structural evolutions during the "hydrothermal potassiation" reaction process. b) Schematic illustration of the fabrication process for K^+-intercalated layered Fe/Mn-based oxide materials. c) Schematic illustration of ion-exchange process. K-birnessite is transformed to H-birnessite by reacting with $(NH_4)_2S_2O_8$, and then turned to TMA-birnessite by further reacting with TMAOH solutions. d) Schematic illustration of expanded intercalated structure of polyaniline-intercalated MnO_2. e) Proposed mechanism for preintercalation of Na^+ ions into MnO_2 interlayers. a) Reproduced with permission.[55] Copyright 2019, Wiley-VCH. b) Reproduced with permission.[50] Copyright 2017, Elsevier. c) Reproduced with permission.[49] Copyright 2017, Elsevier. d) Reproduced under the terms of the CC-BY Creative Commons Attribution 4.0 International license (https://creativecommons.org/licenses/by/4.0).[24] Copyright 2018, The Authors, published by Springer Nature. e) Reproduced with permission.[58] Copyright 2013, Springer Nature.

of multivalent ions (i.e., Zn^{2+}, Mg^{2+}, etc.), due to the high desolvation energy of multivalent ions.[51]

Generally, the large-size organic ions/ molecules are difficult to be intercalated into the interlayer space of layered MnO_2 via the above two synthesis methods, thus, the ion-exchange reaction and aqueous/organic interfacial reaction are applied to overcome this obstacle. For instance, Wang el al.[45] obtained the tetramethyl ammonium (TMA^+) ions intercalated layered δ-MnO_2 via ion-exchange reaction between the H^+-intercalated layered MnO_2 and TMAOH, in which the neutralization reaction between the intercalated H^+ and OH^- ions in the TMAOH result in the preintercalation of TMA^+ ions into the interlayer space of the layered MnO_2 (Figure 1c). The synthesis reaction is as the reactions in Equations (4) and (5)

$$K_{0.25}MnO_2 + 0.25H^+ \rightarrow H_{0.25}MnO_2 + 0.25K^+ \quad (4)$$

$$H_{0.25}MnO_2 + 0.25TMA - OH \rightarrow TMA_{0.25}MnO_2 + 0.25H_2O \quad (5)$$

The TMA^+ intercalated δ-MnO_2 presented an expanded layer spacing of 0.97 nm, which greatly enhanced the diffusion kinetics of hydrated Mg^{2+} (higher rate performance). Huang et al.[24] reported a polyaniline-intercalated layered MnO_2 synthesized by the aqueous/ organic interfacial reaction, in which they conducted the chemical oxidation polymerization of aniline and the reduction of MnO_4^{2-} at the interface of the organic phase (i.e., CCl_4-containing aniline monomer) and the inorganic phase (i.e., $KMnO_4$ aqueous solution) to produce the polyaniline-intercalated layered MnO_2 (Figure 1d). The corresponding synthesis reaction is as the reaction in Equation (6)

$$x\mathrm{KMnO_4\,(in\,water)} + 3n\mathrm{C_6H_7N\ in\ CCl_4} \rightarrow (\mathrm{C_6H_6N})_{3n}(\mathrm{MnO_2})_x + x\mathrm{KOH} + x\mathrm{H_2O} \quad (6)$$

Due to the polymer-strengthened layered structure, the phase changes are largely eliminated, leading to a long-term stability over 5000 cycles with capacity utilization of 40%. The above two preintercalation methods can significantly expand the layer spacing of MnO_2 materials to enhance the diffusion kinetics as well as the structural stability. However, the complicated synthesis processes make it difficult to achieve large-scale industrial production.

Furthermore, for the electrodeposition method, Mai et al.[58] reported that the sodium preintercalation could be carried out by anodically galvanostatic electrodeposition in a solution containing Mn (II) salts, and Na_2SO_4 additives (Figure 1e). This electrodeposition reaction is the reaction in Equation (7)

$$Mn^{2+} + xNa^+ + 2H_2O \rightarrow Na_xMnO_2 + (2-x)e^- + 4H^+ \quad (7)$$

The sodium intercalated Na_xMnO_2 nanoflake based supercapacitors exhibited faster ionic diffusion with enhanced redox peaks, tenfold-higher energy densities up to 110 Wh kg^{-1}, and higher capacitances over 1000 F g^{-1} than that of the traditional MnO_2 supercapacitors, indicating that preintercalation of alkaline ions could activate more active sites for electrochemical adsorption/desorption of carrier ions. The electrodeposition method is simple, fast, and very suitable for the large-scale preparation of preintercalated MnO_2, however, the electrodeposited MnO_2 is usually amorphous, and lacks tunnels for diffusion of carrier ions inside crystal structures of MnO_2 materials, which makes it difficult to be used as cathodes in battery applications.

3. Enhancing Intrinsic Electronic/Ionic Conductivity

The intrinsic electronic/ionic conductivity of cathode materials is usually considered as critical parameters for the electrochemical charge storage of MnO_2 material, which is closely related to the electronic structure of the materials.[59] MnO_2 is a wide bandgap semiconductor with low electrical conductivity.[60] To optimize the intrinsic conductivity of MnO_2, some strategies have been developed, including transition metal-doping, defect engineering, preintercalation, etc.[61–62] Preintercalation was regarded as one of the most effective methods to enhance the electronic/ionic conductivity due to the optimized electronic structure of MnO_2, and thus consequently lead to higher electrochemical performance.

The preintercalation effect of preintercalated ions on the conductivity of MnO_2 have been massively investigated, including Na^+ intercalated layered MnO_2,[63–65] V-intercalated MnO_2 nanosheets,[66] Ce^{3+}-intercalated MnO_2,[57] K^+ intercalated α-MnO_2,[67,68] Cu^0-intercalated birnessite MnO_2,[69] Zn^{2+} intercalated δ-MnO_2,[70] and Na^+ intercalated α-MnO_2,[71] etc. We observe that the structural optimizations of MnO_2 materials induced by preintercalation give rise to significant changes in electronic and ionic conductivity. For instance, Young et al.[60] revealed that the intercalated cations in α-MnO_2 could induce charge-switching states by stabilizing Mn—O antibonding orbitals from the conduction band, and thus the bandgap between the valence and conductive bonds could be reduced to obtain higher electronic conductivity. Ye et al.[64] have attributed the enhanced capacitive performances of MnO_2 to the improvement in Na^+ diffusion coefficient and electrical conductivity via preintercalated Na^+ ions. Thus, a specific capacitance (based on Na^+-intercalated MnO_2) of 295 F g^{-1} at a current density of 1 A g^{-1} was obtained in aqueous Na_2SO_4 solution. Chen et al.[57] reported the Ce^{3+} preintercalation in α-MnO_2 with a 10-fold higher specific capacitance (101 F g^{-1} at 1 A g^{-1}) than that of the pristine MnO_2. With V^{3+} ions intercalated in 2 × 2 tunnels of α-MnO_2, the Fermi energy level of α-MnO_2 increased, and the bandgaps got narrowed with some impurity peaks generating within the bandgap, resulting in the improved electrical conductivity of α-MnO_2 (**Figure 2**a,b).[66] To verify the simulation, the electronic conductivity of MnO_2 samples with different preintercalated V contents was measured using a four-point probe method, and Figure 2c shows the increasing electronic conductivity with the increasing V contents. As a result, the 2D V-intercalated MnO_2 displayed an obviously higher specific capacitance of 439 F g^{-1} at a current density of 0.5 A g^{-1} (Figure 2d).

For K^+ intercalated α-MnO_2, the effect of K^+ on electronic and ionic conductivities of α-MnO_2 have been studied using DFT calculations by Yuan et al.[22]. They found that a newly formed occupied state appeared inside the bandgap of the original α-MnO_2, indicating a mixed Mn^{4+} and Mn^{3+} in $K_{0.25}MnO_2$, and thus the electronic conductivity of α-MnO_2 was effectively enhanced via electron hopping between Mn^{4+}/Mn^{3+}.

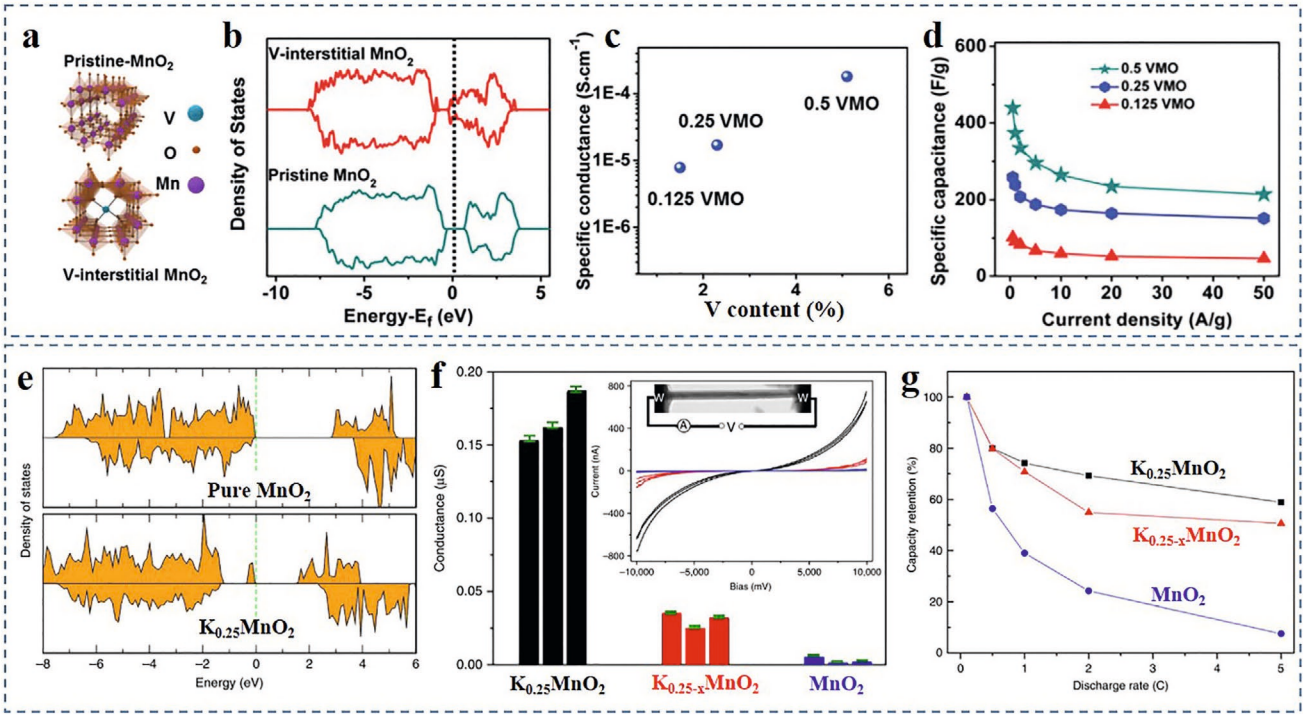

Figure 2. Promoting effect preintercalated cations on intrinsic conductivity of tunneled α-MnO_2. a) Crystal structures and b) density of states (DOS) of the pristine and V intercalated α-MnO_2, and c,d) corresponding specific conductance (c) and specific capacitance (d) of samples. e) Calculated DOS near the Fermi level region of $K_{0.25}MnO_2$ and pure MnO_2; f) conductance of α-MnO_2 nanowires with different K^+ concentrations; and g) effect of K^+ concentration on rate performance of α-MnO_2 nanowires as the cathode of a lithium-ion battery. a–d) Reproduced with permission.[66] Copyright 2015. Royal Society of Chemistry. e–g) Reproduced under the terms of the CC-BY Creative Commons Attribution 4.0 International license (https://creativecommons.org/licenses/by/4.0).[22] Copyright 2016, The Authors, published by Springer Nature.

The electronic conductivity was dramatically improved by the preintercalated K^+ (Figure 2e,f), which was beneficial for ionic conductivity of Li^+ in the tunnels with the presence of K^+. As a result, $K_{0.25}MnO_2$ showed higher capacity delivery as well as more superior rate performance than that of pure MnO_2 (Figure 2g). Xu et al.[71] reported similar results in Na^+ intercalated α-MnO_2, which also presented enhanced electronic conductivity through the electron hopping between Mn^{3+}/Mn^{4+} induced by the preintercalated Na^+ ion. However, it doesn't mean that the more K^+ intercalated, the better the ionic conductivity of α-MnO_2 is. Poyraz et al.[67] indicated that the presence of excess K^+ in 2×2 tunnels of α-MnO_2 may impede the Li^+ diffusion, and samples with lower K^+ content in the initial structure yielded higher specific capacity and improved capacity retention during cycling.

Besides, this preintercalation strategy on enhancing electronic conductivity can also be applied on the layered MnO_2. A very special Cu^0 coexisted with Cu^{2+} in the layered Cu-δ-MnO_2 material was successfully synthesized (**Figure 3**a) by Li et al.[69], in which the presence of a small amount of Cu^0 (identified by XPS method in Figure 3b) improved the conductivity of δ-MnO_2, leading to a low charge transfer resistance and higher Li^+ diffusion kinetics, and thus resulted in better rate performances (Figure 3c). The existence of the free electron Cu^0 acts as electron donors to change the electronic structure of MnO_2 for a better conductivity, similar to the result reported by Kang et al.[72]. Radhamani et al.[70] synthesized various kinds of Zn^{2+} preintercalated δ-MnO_2 samples (Figure 3d), and revealed that δ-MnO_2 with 1% preintercalated Zn^{2+} ions (1Zn-δ-MnO_2) presented the lowest bandgap of ≈2.2 eV, which was much lower than that of pure δ-MnO_2 (≈2.8 eV), indicating an increased electronic conductivity (Figure 3e). Thus, 1Zn-δ-MnO_2 displayed the highest capacitance, as well as highest rate performance (Figure 3f). Xia et al.[65] reported that the bandgap of monoclinic Na^+-δ-MnO_2 presented a low value of ≈1.25 eV, indicating an excellent electronic conductivity of this material. They also introduced oxygen vacancies (≈4.0 at%) into the lattice of Na^+–MnO_2 via annealing in Ar atmosphere, as a result, further enhancement on the electronic conductivity of $NaMnO_2$ was achieved (Figure 3g,h).

In summary, the preintercalation effect on enhancing electronic/ionic conductivity of MnO_2 materials can be summarized as follows: i) the preintercalation of cations can increase the Fermi energy level, and decrease the bandgap of α-MnO_2, thus improving the electrical conductivity; ii) the enhanced electronic conductivity of MnO_2 is mainly attributed to the electron hopping between Mn^{3+}/Mn^{4+} induced by K^+/Na^+ preintercalation; iii) there exist an optimum concentration of the preintercalated cations for enhancing conductivity of MnO_2; iv) preintercalation of cations expands the tunnel/layer size, which facilitate the ionic conductivity of MnO_2; v) further enhancement on conductivity of MnO_2 can be achieved by introducing oxygen defects accompanied by the preintercalation of cations; vi) the intercalated free electron metal atoms act as electron donator to change electronic structure of MnO_2 materials for better electronic conductivity.

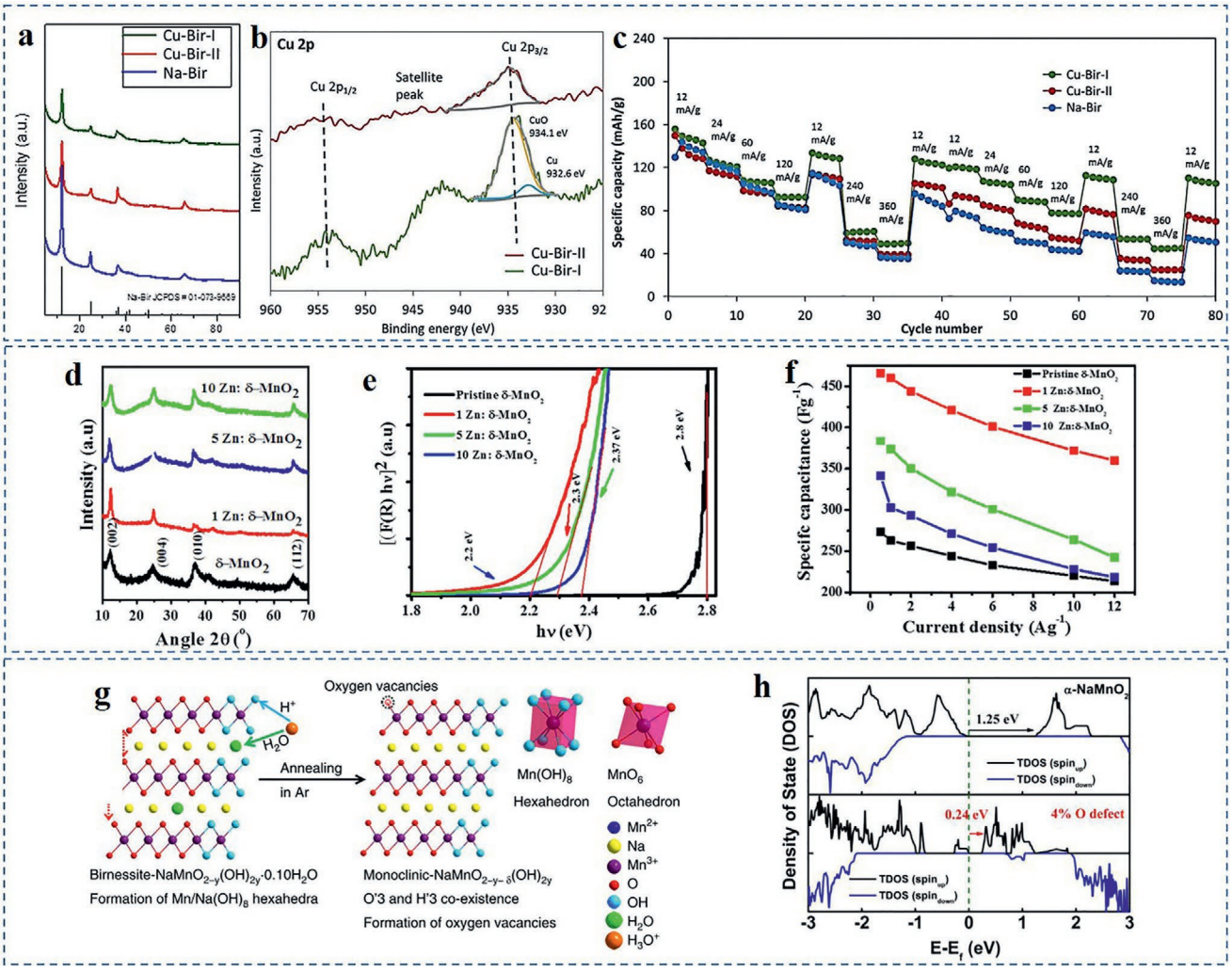

Figure 3. Promoting effect of the preintercalation strategy on intrinsic conductivity of layered MnO_2. a) XRD patterns of Cu-Bir-I, Cu-Bir-II, and Na-Bir (where Cu-Bir-I = $Cu^0_{0.03}Cu^{2+}_{0.21}Na_{0.12}MnO_2{\cdot}0.9H_2O$, Cu-Bir-II = $Cu_{0.26}MnO_2{\cdot}1.0H_2O$; and Na-Bir = $Na_{0.40}MnO_2{\cdot}0.9H_2O$); b) XPS analysis of Cu 2p spectrums for Cu-Bir-I and Cu-Bir-II samples; and c) corresponding comparison of rate performances. d) XRD patterns and e) plots of $[F(R)h\nu]^2$ versus $h\nu$ for pristine and Zn^{2+}-intercalated δ-MnO_2 cathodes, giving the bandgap values; f) corresponding comparison of rate performances. g) Schematic illustration of generation of δ-Na^+–δ-MnO_2 with oxygen vacancies, and h) calculated DOS of α-$NaMnO_2$ and α-$NaMnO_{2-\delta}$ with 4% oxygen vacancies. a–c) Reproduced with permission.[69] Copyright 2017, IOP Science. d–f) Reproduced with permission.[70] Copyright 2018, Elsevier. g,h) Reproduced under the terms of the CC-BY Creative Commons Attribution 4.0 International license (https://creativecommons.org/licenses/by/4.0).[65] Copyright 2018, The Authors, published by Springer Nature.

4. Activating More Active Sites for Charge Storage

MnO_2 materials have been widely investigated as cathode materials in batteries and supercapacitors. By reviewing literatures, we conclude that the preintercalation can effectively increase the density of electrochemical "active sites" for charge storage of MnO_2, thus, it can increase the capacity/capacitance of batteries/ supercapacitors. This "active sites" is a collective name of electrochemical active binding sites for both the charge diffusion and storage in batteries and redox/insertion-type pseudocapacitance in supercapacitors. When used as cathodes in batteries, the preintercalation helps the carrier ions to diffuse deeper (mainly via decreasing energy barrier for diffusion of charge ions) into the lattice structure of MnO_2 electrodes and activates more active sites, especially under high-rate currents.[73,74] For example, the intercalated K^+ could promote the Li^+ diffusion in 2×2 tunnels of α-MnO_2 to occupy more active sites (forming Mn—O—Li bonds), which contributed to the superior rate performance;[22] Liu et al.[23] reported that the K^+ in α-MnO_2 facilitates the H^+/Zn^{2+} diffusion and subsequent chemical binding with more active sites (forming Mn—O—H/Zn bonds) in MnO_2 in a mild aqueous media. As a result, the $K_{0.19}MnO_2$ cathode exhibited a high capacity of 113 mA h g^{-1} at 20 C, while the $K_{0.07}MnO_2$ cathode only showed a capacity of 12 mA h g^{-1} at the same current density. Also, the intercalated Mg^{2+} ions in MnO_2 increased the corresponding Mg^{2+} diffusion coefficient, leading to a higher capacity delivery of the MnO_2 cathodes,[73] the as-prepared $Mg_{1.1}Mn_6O_{12}{\cdot}4.5H_2O$ cathode achieved a high capacity of 248.8 mAh g^{-1} at 10 mA g^{-1}. This increased density of active sites for MnO_2 cathode in batteries (i.e., high capacity) is mainly attributed to the promoted diffusion kinetics from preintercalation, which will be discussed in the later section.

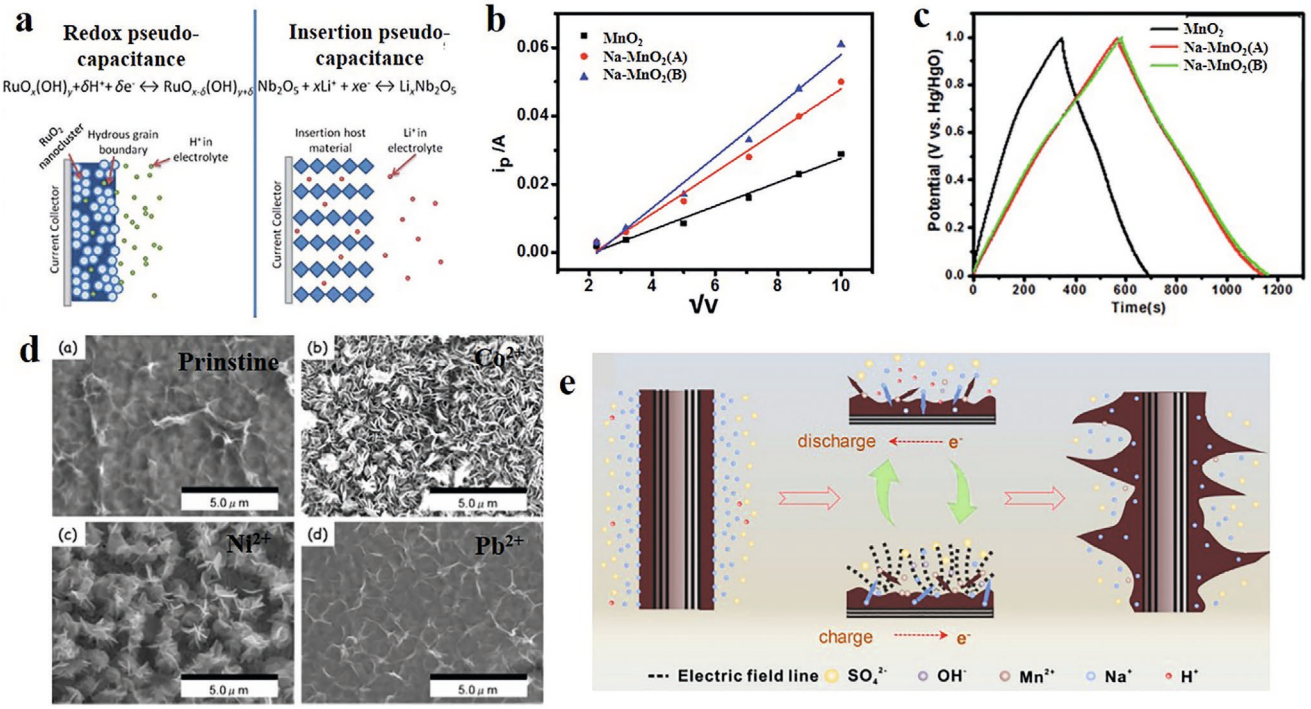

Figure 4. Effect of preintercalated cations on redox-type pseudocapacitance of MnO_2. a) Schematic illustration of the redox/insertion pseudocapacitance. b) Peak current versus the square root of the scan rate for Na^+-inserted birnessite-MnO_2 and c) corresponding charge–discharge profile of samples at 0.3 A g^{-1}. d) Comparison of SEM morphologies of the Co^{2+}-, Ni^{2+}-, and Pb^{2+}-intercalated MnO_2. e) The structural reconstruction process of Na^+ inserting into MnO_2 during electrochemical cycling. a) Reproduced with permission.[75] Copyright 2014, Royal Society of Chemistry. b,c) Reproduced with permission.[56] Copyright 2015, Royal Society of Chemistry. d) Reproduced with permission.[20] Copyright 2010. The Electrochemical Society, published by IOP Science. e) Reproduced with permission.[80] Copyright 2019, Elsevier.

When used as cathode in supercapacitors, the preintercalation in MnO_2 can improve the active sites to achieve higher redox/insertion-type pseudocapacitance. The redox pseudocapacitance occurs when ions are electrochemically adsorbed onto the surface/near-surface of a cathode material (e.g., RuO_x) with a concomitant faradaic charge-transfer,[75,76] while the insertion pseudocapacitance occurs when ions intercalate into the tunnels or layers of a redox-active material (e.g., Nb_2O_5) accompanied by a faradaic charge-transfer without phase transformation (**Figure 4**a).[77,78] Generally, the preintercalation of ions/ molecules in MnO_2 materials can simultaneously improve the redox-type and insertion-type pseudocapacitance.[71,79] The enhanced redox-type pseudocapacitance by preintercalation is mainly attributed to the increase of BET surface area and controlling morphologies of MnO_2, which result in higher density of active sites on surface of the poorly crystallized MnO_2.[57,80] For example, Chen et al.[57] reported that Ce^{3+} intercalated α-MnO_2 presented much higher BET surface area, which provided more surface active sites to increase redox-type pseudocapacitance; Radhiyah et al.[56] reported that the Na^+ preintercalated δ-MnO_2 showed the doubling of the specific capacitance due to the enhanced BET surface area (Figure 4b), as a result, the Na^+ preintercalated δ-MnO_2 presented nearly double of the specific capacitance comparing with that of pure δ-MnO_2 (Figure 4c); Inoue et al.[20] revealed that the Co^{2+}, Ni^{2+}, and Pb^{2+} preintercalated MnO_2 materials during electrochemical cycling presented remarkably increased specific capacitances, with drastic morphology changes occurring from multilayers lying parallel to the substrate to aligning vertically (Figure 4d), and thus gained much higher amount of active sites responsible for the enhanced capacitance; Sun et al.[80] also reported that the intercalation of electrolyte ions (Na^+) into MnO_2 during electrochemical cycling caused significant changes of morphologies (Figure 4e), as well as the increased capacitance.

Preintercalation can also effectively improve the insertion-type pseudocapacitance of MnO_2 materials, mainly attributing to increased exposure of active sites by the expanding the interlayer spacing or reducing the crystallinity. For instance, Zhao et al.[49] reported that the enhanced insertion-type pseudocapacitance could be obtained by enlarging interlayer spacing of δ-MnO_2 through a controllable preintercalation of K^+, TMA^+, and H^+ cations. An impressively high specific capacitance of 580.05 F g^{-1} was achieved for TMA^+/ H^+ = 1000 sample at current density of 2 A g^{-1}, which was much higher than that of K-birnessite, H-birnessite, TMA^+/ H^+ = 800 (352.8, 414.9, 497.25 F g^{-1}), indicating the critical role of preintercalation strategy on enhancing intercalation-type pseudocapacitance of layered δ-MnO_2. Jabeen et al.[81] revealed that the preintercalated K^+ in α-MnO_2 could be replaced by Na^+, resulting in significantly improved insertion-type pseudocapacitance (**Figure 5**a), i.e., higher amount of active sites was exposed inside 2 × 2 tunnels of α-MnO_2 due to the preintercalated K^+ ions. They also pointed out that the occurrence of Mn^{3+} ions induced by the preintercalated ions in α-MnO_2 was responsible for the additional active sites, associating with the Mn^{3+}/Mn^{4+} redox couple. The K_xMnO_2 electrode showed a high specific capacitance of 260 F g^{-1} at current density of 1 A g^{-1}, which was obviously higher than that of the K^+-free MnO_2 electrode (184 F g^{-1}). Lin et al.[82,83]

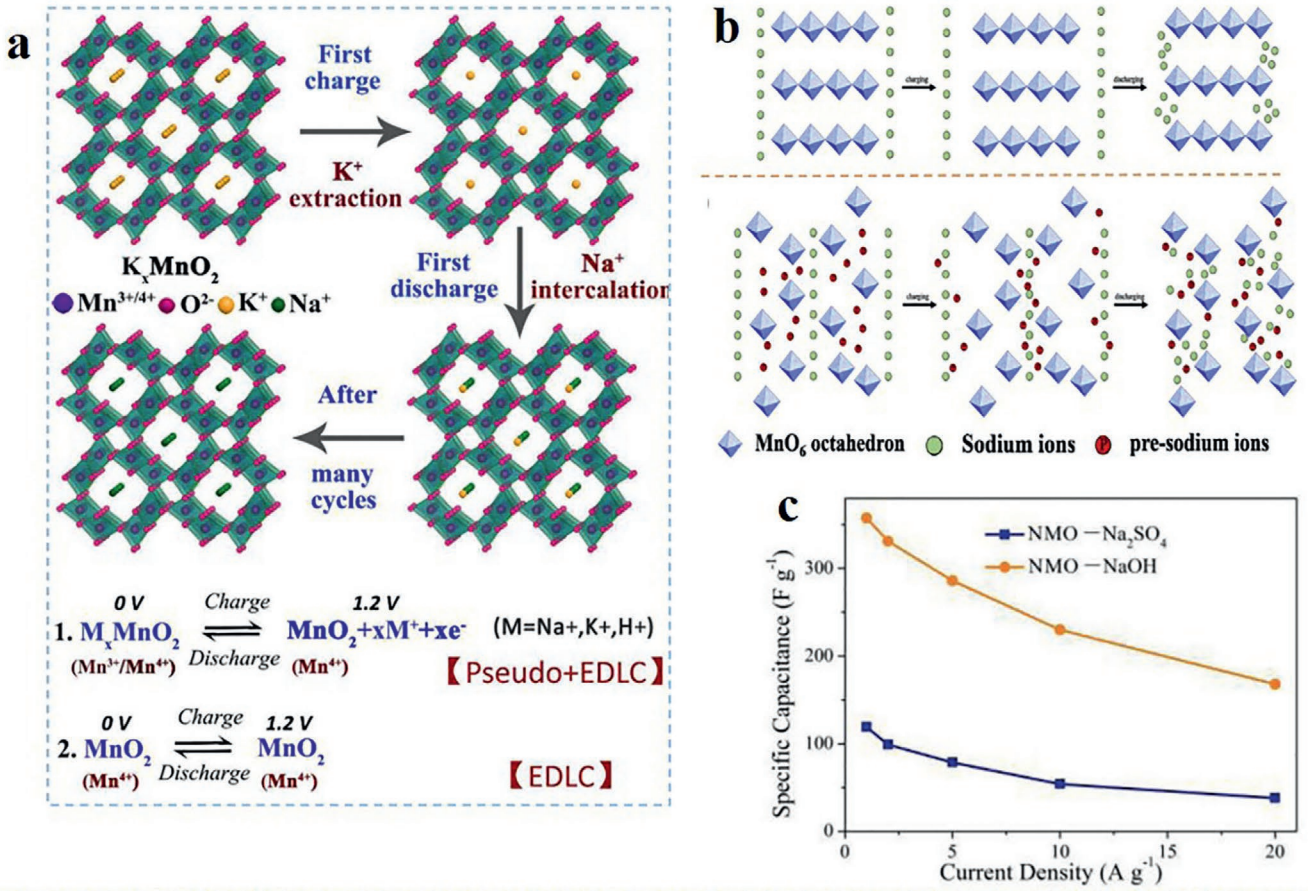

Figure 5. Enhancing effect of preintercalation on insertion-type pseudocapacitance. a) Schematic illustration for the electrochemical reaction process of the K_xMnO_2 electrode and proposed charge-storage mechanisms for M_xMnO_2 and MnO_2. b) Schematic charging/discharging processes for MnO_2 and Na_xMnO_2 with reduced crystallinity. c) Specific capacitance as a function of current density in different electrolytes. a) Reproduced with permission.[81] Copyright 2016, American Chemical Society. b) Reproduced with permission.[83] Copyright 2018, Elsevier. c) Reproduced with permission.[85] Copyright 2018, Wiley-VCH.

investigated the Na^+/K^+ preintercalated δ-phase MnO_2 as positive electrodes in asymmetric supercapacitors, they found that the crystallinity of MnO_2 materials was significantly reduced by the preintercalation of Na^+/K^+ into its layered structure (Figure 5b), which benefited to the Na^+/K^+ diffusion into/out the interlayer structure, leading to effective utilization of the active sites inside the crystal structure of MnO_2 cathode. Besides, the preintercalation effect is also significantly affected by the electrolyte compositions. Chen et al.[84] investigated the capacitive characteristics of $Na_{0.3}K_{0.03}MnO_{1.57}$ and $K_{0.29}MnO_{1.58}$ in aqueous neutral electrolytes containing various cations, and revealed that the capacitive responses of both oxides are significantly affected by the electrolyte ions because of the influences of conductivity, pH, charge-to-mass ratio, ionic radius, primary and secondary hydrated radii, as well as hydration ratio. Zhang et al.[85] reported a $Na_{0.55}Mn_2O_4\cdot 1.5H_2O$ (NMO) cathode which presented much higher specific capacitance in NaOH electrolytes (358 F g^{-1} at 1 A g^{-1}) than that in Na_2SO_4 electrolyte (119 F g^{-1} at 1 A g^{-1}) (Figure 5c).

Based on the above results, preintercalation can activate more active sites for the charge storage (or expand the charge/discharge depth) of MnO_2 materials, and the correlated reasons are summarized as follows: i) when used as cathode in batteries, the preintercalation helps the carrier ions to diffuse deeper via decreasing diffusion energy barrier inside the interlayers/tunnels of the MnO_2, and supplies more binding sites for carrier ions; ii) when used as cathodes in supercapacitors, preintercalation can activate more active sites for both redox and insertion-type pseudocapacitances; iii) the enhanced redox-type pseudocapacitance by preintercalation is mainly attributed to the increase of BET surface area and controlling morphology of MnO_2 materials; iv) the improved insertion-type pseudocapacitance of MnO_2 is mainly due to the expansion of the interlayer spacing or reducing the crystallinity, which increased the amount of active sites. Hence, the preintercalation is suggested to be an effective way to provide additional active sites to accept cations for MnO_2-based electrodes, no matter in batteries or supercapacitors applications, and this enhancing effect is a combined effect of tuning conductivity, diffusion coefficient, phase structure, as well as micro-morphology of MnO_2.

5. Promoting Diffusion Kinetics

5.1. Strategies Promoting Intrinsic Diffusion Kinetics of MnO_2

The ionic diffusion kinetics is a key factor for rechargeable MnO_2 cathodes. It is well known that the diffusion kinetics of the

carrier M^{n+} ions (M^{n+} = H^+, Li^+, Na^+, Zn^{2+}, Mg^{2+}, etc.) in MnO_2 electrodes is determined by many factors, including carrier ion species, crystalline structure, vacancy concentration, as well as the phase transformation during cycling.[86,87] Despite these complicated factors, the diffusion of carrier ions is mainly dominated by the value of the electrostatic repulsion (f) between the carrier ions and anion framework of MnO_2. Generally, the f is linearly variated with the value of $1/(\varepsilon_r r_0^2)$, where ε_r is the permittivity, and the r_0 is the distance between the inserted carrier ion and the neighboring oxygen ions of host framework.[88] Thus, there exist two effective routes enhancing the intrinsic diffusion kinetics of MnO_2: i) reducing effective charge of carrier ions via charge shielding effect of crystal water; ii) expanding interlayer spacing to achieve higher r_0, decreasing the electrostatic repulsion between carrier ions and host framework and thus enhancing diffusion. Preintercalation of crystal H_2O, ions, and other organic species provides an ideal path to reduce effective charge of carrier ions, or to expand the interlayer spacing or tunnel size of MnO_2 materials, or to achieve both of the above two aspects.

5.2. Charge Shielding Effect of Crystal Water

To reduce the electrostatic interaction of the carrier ions and anion framework, structural water was introduced to partially shield the charge of monovalent ions (e.g., Li^+, Na^+, etc.) or multivalent ions (e.g., Mg^{2+}, Zn^{2+}) when they diffuse through the layered or tunnel structure of MnO_2 materials. An ideal explanation for the charge shielding effect of crystalline water was proposed by Frey et al.[52]. They found that the strong electrostatic interaction (via Bader charge analysis) between the dipolar water molecule and the positively charged Na^+ ions inside a 2 × 3-MnO_2 tunnel structure ($Na_{0.2}MnO_2 \cdot 0.2H_2O$) (**Figure 6**a) led to a partial negative charge of ≈0.6 e^- localized on the oxygen atom in the water molecule, and thus reduced the "effective charge" of Na^+, resulting in the decreased electrostatic bond strength. DFT results presented that the discharge insertion potential for one water and two Na^+ ions (2.97 V vs Na/Na^+) were higher than the case of no water and two Na^+ ions (2.76 V vs Na/Na^+), which demonstrated the crucial role of crystal water on facilitating the Na^+ diffusion in tunnels of MnO_2. Meanwhile, DFT results also indicated that a –0.25 V penalty was introduced by the ion–lattice interaction induced lattice strain, while a 0.50 V increase resulted from a hydrogen-bonding-like interaction between crystal water and Na^+ ions, thus, a 0.25 V increase in the insertion voltage after hydration was obtained (Figure 6b), which was in good agreement with the experimental results. Furthermore, Nam et al.[51] reported the Na^+ insertion/extraction behavior in a Na^+ and H_2O cointercalated layered framework ($Na_{0.71}MnO_2 \cdot 0.25H_2O$), where the crystal H_2O substantially improved the Na^+ diffusion in both the host lattice and at the electrode-electrolyte interface (Figure 6c). They also revealed that the impedance measured with $Na_{0.71}MnO_2 \cdot 0.25H_2O$ (i.e., 613 Ω cm^2 for 1st semicircle of EIS) was by orders of magnitude lower compared to that of the heat-treated $Na_{0.71}MnO_2$ (i.e., 154 680 Ω cm^2 for 1st semicircle of EIS) (Figure 6d), which was attributed to charge shielding effect of crystal water in the host structure, as well as the expanded interlayer spacing. The crystal water facilitated Na^+ transport by compensation for the loss of the solvation shell of Na^+

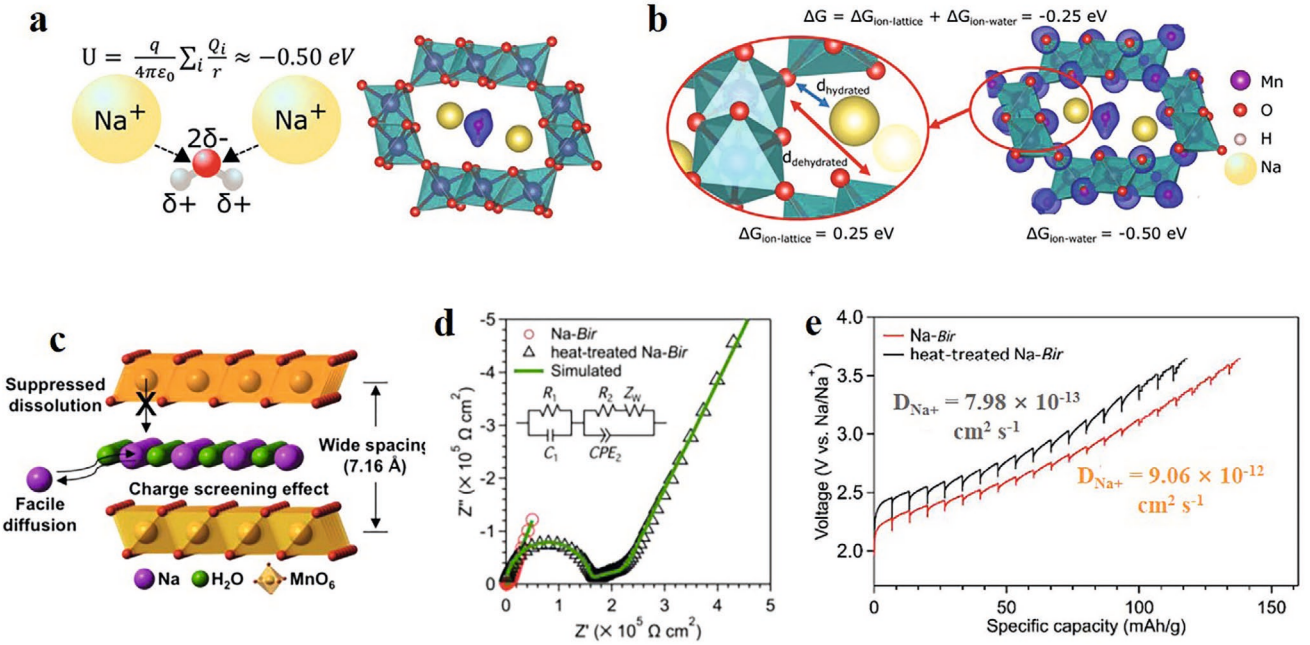

Figure 6. Charge-shielding effect of crystal water. a) The electrostatic interaction between positively charged Na^+ ions and the dipolar water molecule, and b) the charge density after hydration, where the Na^+–water interaction results in a contribution of ≈–0.50 eV to the Gibbs free energy and strain effects induce an energy penalty of ≈0.25 eV, resulting in a total change in the Gibbs free energy upon hydration of ≈–0.25 eV. c) Crystal structures of Na-Bir with charge shielding effect to promote the diffusion of Na^+ ions, d) comparison of EIS plots of Na-Bir electrodes with/without crystal water, and e) enhanced diffusion kinetics of Na^+ ions of Na-Bir with crystal water. a,b) Reproduced with permission.[52] Copyright 2018, Royal Society of Chemistry. c–e) Reproduced with permission.[51] Copyright 2015, American Chemical Society.

ions in the transfer from the solution to the solid phases, as a result, the diffusion coefficient (D_{Na+}) of $Na_{0.71}MnO_2 \cdot 0.25H_2O$ (9.06×10^{-12} cm^2 s^{-1}) was much higher than that of the heat-treated $Na_{0.71}MnO_2$ (7.98×10^{-13} cm^2 s^{-1}) (Figure 6e). Thus, by applying the charge shielding effect of crystal water, the diffusion kinetics of Na^+ can be enhanced for improved electrochemical rate performance in Na-ion batteries. This principle can also be applied to the use of manganese oxides in batteries based on other monovalent carrier ions, such as Li-ion,[89] and K-ion batteries.[90]

The charge shielding effect of crystal water is more favorable for the charge storage and transport of multivalent ions (e.g., Mg^{2+}, Zn^{2+}) for MnO_2 cathode. Due to the strong electrostatic repulsion between the Mg^{2+}/Zn^{2+} ions and the host frameworks cathodes, the sluggish diffusion kinetics of Mg^{2+}/Zn^{2+} ions in various cathode materials remains a bottleneck for developing high-performance Mg/Zn-ion batteries.[13,91] In addition to reducing the particle size of cathode materials to decrease the diffusion length of ions, utilizing the charge shielding of crystal water in electrolyte or in interlayer space provides a good way to reduce this electrostatic resistance to obtain higher diffusion kinetics.[92] Levi et al.[91] first proposed (in 2010) that a hybrid preintercalation compounds containing crystal H_2O or other additional anion groups could presumably screen the charge of the inserted Mg^{2+} cations. Mai's group[93,94] reported the charge shielding effect of crystal water on enhancing diffusion kinetics of Mg^{2+} ions in $Mn_{0.04}V_2O_5$ $1.17H_2O$ and $Mg_{0.3}V_2O_5$ $1.1H_2O$ cathodes. Multiple kinds of MnO_2 containing crystal H_2O have been investigated as cathode materials for Mg^{2+} insertion/extraction, including α-MnO_2,[14,42] γ-MnO_2,[95] δ-MnO_2,[96] λ-MnO_2,[97] todorokite-type MnO_2,[73] and so on. Song et al.[96] reported that MnO_2 electrode could be "activated" for Mg^{2+} insertion/extraction by cycling in water containing electrolyte even with the absence of crystal H_2O, i.e., after the electrochemically preintercalating crystal H_2O, the MnO_2 electrode showed an initial capacity of 120 mA h g^{-1} (@0.4 C) in dry Mg electrolyte, which was comparable to that in aqueous solution. Nam et al.[98] adopt an unconventional approach of engaging crystal water in the layered structure of δ-MnO_2. They confirmed the crucial role of crystal H_2O by directly visualizing its presence and dynamic rearrangement using STEM, and revealed that the crystal H_2O could effectively screen electrostatic interactions between inserted Mg^{2+} and the host anions, and led to a high capacity delivery of 231.1 mAh g^{-1} at 100 mA g^{-1} and a superior rate performance with a capacity retention of 48.6% at 2000 mA g^{-1} (**Figure 7**a,b). In contrast, the heat-treated Mg-δ-MnO_2 (the crystal H_2O is removed) exhibited larger overpotentials, smaller capacities, and inferior cycling performance, which could all be attributed to the decreased diffusion kinetics of Mg^{2+} ions after the removal of the crystal H_2O. Besides, they also added various amounts of H_2O to the nonaqueous electrolytes, and found that the hydrated Mg^{2+} ions were easily inserted into the hosts while retaining the hydration to a large extent, and thus decreased the de-solvation energy penalty as well as the coulombic repulsion at the host interface. In addition to the shielding provided by the crystal H_2O, the hydration of Mg^{2+} ions would allow for continuous shielding against the host even after insertion.

Similarly, the charge shielding effect of crystal H_2O to screen the electrostatic interactions between Zn^{2+} ions and the host framework has also been widely reported for the layered

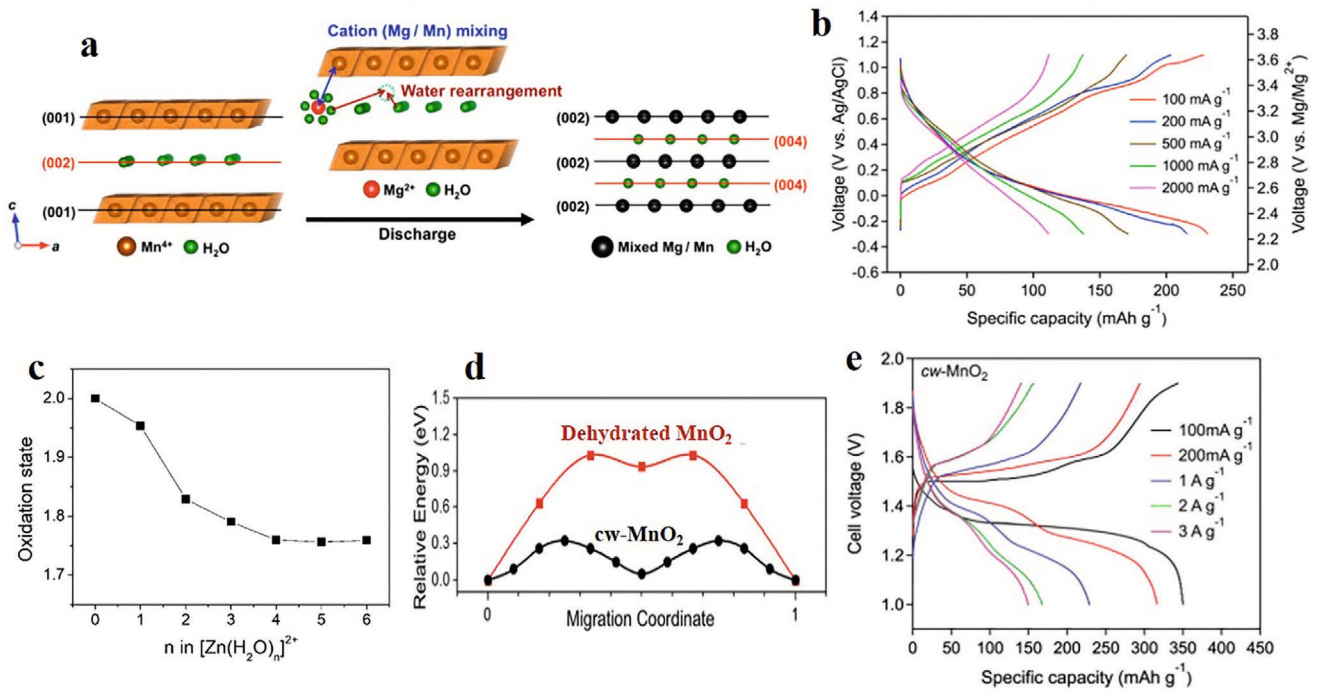

Figure 7. a) Illustration of insertion of hydrated Mg^{2+} in a Mg-Bir cathode and Mg/Mn mixing during discharge process, and b) corresponding rate performance. c) Oxidation state of Zn center as a function of the number of coordinate water molecules, d) the Zn-ion migration barriers in the cw-MnO_2, and dehydrated MnO_2 cathodes, and e) corresponding rate performance of cw-MnO_2. a,b) Reproduced with permission.[98] Copyright 2015, American Chemical Society. c–e) Reproduced with permission.[99] Copyright 2019, Royal Society of Chemistry.

vanadium oxide cathodes, including $Zn_{0.25}V_2O_5 \cdot nH_2O$ nanobelts,[100] $Co_{0.247}V_2O_5 \cdot 0.94H_2O$ nanowires,[101] $V_2O_5 \cdot nH_2O$,[102] bilayer $V_2O_5 \cdot nH_2O$,[88] and so on. However, the charge shielding effect of crystal H_2O for layered MnO_2 cathodes is relatively less reported. In fact, the crystal H_2O in tunnels or interlayers of MnO_2 materials can also facilitate the Zn^{2+} diffusion utilizing the charge shielding effect. Lee et al.[103] reported that the crystal H_2O in large 3×3 tunnels of todorokite MnO_2 could reduce the electrostatic interaction between the inserted Zn^{2+} ions and MnO_2 framework, thus ensured faster Zn^{2+} diffusion in aqueous Zn batteries. When used as cathodes for aqueous zinc ion batteries, the δ-MnO_2 without crystal H_2O only exhibited a low capacity of 133 mAh g^{-1} at a current density of 100 mA g^{-1}, indicating an insufficient Zn^{2+} insertion upon discharge.[104] With crystal H_2O (10 wt%), the hydrated δ-MnO_2 exhibited a high reversible capacity of 350 mAh g^{-1} at 100 mA g^{-1}, along with excellent cycling and rate properties, as reported by Nam et al.[99] DFT calculations illustrated that the charge transfer from the coordinated H_2O to Zn^{2+} center was estimated to be ≈0.25 electrons when the coordination number of H_2O varied among 4–6 (Figure 7c), thus the effective charge of Zn^{2+} was reduced to achieve lower electrostatic repulsions on Zn^{2+} ion by shielding its positive charge. The Zn migration barrier in this hydrated δ-MnO_2 was about 0.32 eV, which was substantially lower than that of the dehydrated case (1.03 eV), as shown in Figure 7d, supporting the facile migration of Zn^{2+} ions in the hydrated δ-MnO_2. Due to the charge shielding effect of H_2O and the expanded interlayer spacing, the δ-MnO_2 containing ≈10 wt% of crystal H_2O (150.0 mA h g^{-1} @ 3 A g^{-1}, Figure 7e) presented much higher rate property than that of the heat-treated δ-MnO_2 (24.0 mA h g^{-1} @ 3 A g^{-1}).

5.3. Expanding Interlayer Spacing

In addition to the charge shielding effect of crystal H_2O, expanding interlayer spacing (or size of tunnels) has also been applied to facilitate diffusion kinetics of carrier ions.[36,48] For various kinds of cathode materials, including V_2O_5, MnO_2, etc., larger diffusion tunnels induced by preintercalation of cations and molecules benefit a lot to achieve higher diffusion kinetics of carrier ions.[19,38] For MnO_2 materials based on the monovalent ions (Li^+, Na^+, K^+, etc.), it is reported that the D_{Li+} values for α-MnO_2 with preintercalated K^+ ions vary from 1×10^{-10} cm^2 s^{-1} at fully charged state to 2×10^{-11} cm^2 s^{-1} at fully discharged state,[105] while for the todorokite-type MnO_2, the D_{Li+} values is $\approx 1 \times 10^{-7}$ cm^2 s^{-1} at fully charged state, and 3×10^{-10} cm^2 s^{-1} at fully discharged state.[106] Yuan et al.[22] reported that the D_{Li+} of α-$K_{0.25}MnO_2$ (1.91×10^{-12} cm^2 s^{-1}) was several orders of magnitude higher than that of pure α-MnO_2 (2.82×10^{-15} cm^2 s^{-1}), mainly due to the expanded diffusion tunnel size and increased electronic conductivity via preintercalated K^+ ions. For the diffusion kinetics of Na^+ ions, Li et al.[107] reported that the crystal water containing Na-birnessite with an enlarged interlayer distance of 7.15 Å exhibited higher diffusion rate of Na^+ in the crystal structure and at the electrode/electrolyte interface, comparing with that of the α-$NaMnO_2$ (5.26 Å). Zhao et al.[49] developed an effective strategy to synthesize the layered MnO_2 with enlarged interlayer spacing through a controllable preintercalation of K^+, H^+, TMA^+/H^+ and TMA^+ cations for electrochemical Na^+ storage (**Figure 8**a). The δ-MnO_2 electrode with $TMA^+/H^+ = 1000$ showed the highest Na^+ storage ability and rate performance (Figure 8b), mainly due to the expansion of interlayer spacing caused by TMA^+ intercalation, which weakened electrostatic interaction, and facilitated the Na^+ diffusion. The authors use the Warburg resistance (Z_w) to correlate the diffusion of Na^+ ions, and $TMA^+/H^+ = 1000$ preintercalated δ-MnO_2 shows much sharper Warburg plot than that of K^+ and H^+ preintercalated δ-MnO_2, indicating faster diffusion of Na^+ ions (Figure 8c). Similarly, Zhang et al.[85] reported that the preintercalated Na^+ ions could increase the interlayer spacing and thus promoted the diffusion of Na^+ ions within the layers.

However, the diffusion of carrier ions was influenced by both the size and valence of the preintercalated cations and their electrostatic reaction with the carrier ions. Lu et al. investigated the effect of intercalated cation species (e.g., Li^+, Na^+, K^+, Co^{2+}, and Mg^{2+}) on Li^+ and Na^+ storage of layered MnO_2 materials.[26] The specific capacities of Li–MnO_2, Na–MnO_2, K–MnO_2, Mg–MnO_2, and Co–MnO_2 were about ≈118, ≈137, ≈155, ≈97, and ≈87 mAh g^{-1} for Li^+ storage and ≈75, ≈145, ≈113, ≈65, and ≈46 mAh g^{-1} for Na^+ storage, and thus clearly showing cation-dependent diffusion kinetics. Although the Mg–MnO_2 and Co–MnO_2 had larger interlayer spacing, they delivered lower capacities for both Li^+ and Na^+ storage due to the enlarged diffusion barriers. Thus, for δ-MnO_2 pillared by monovalent cations, the diffusion was enhanced by the expansion of the interlayer spacing, while for δ-MnO_2 pillared by divalent cations, the diffusion was influenced by both the interlayer spacing and the potential electrostatic repulsion forces between preintercalated cations and carrier ions. Simultaneously, the amount of intercalated cations in layered MnO_2 also affected the diffusion of carrier ions. Cao et al.[108] reported that the amount of preintercalated K^+ could be adjusted by changing the amount of $KMnO_4$ (from 3 to 7 mmol) in synthesis process (Figure 8d). On one hand, introducing K^+ into MnO_2 structure resulted in an expansion of interlayer spacing, which enhanced the K^+ diffusion in MnO_2 with D_{K+} increasing from 2.66×10^{-9} cm^2 s^{-1} ($K_{0.14}MnO_2$) to 8.92×10^{-9} cm^2 s^{-1} ($K_{0.19}MnO_2$); on the other hand, once the amount of preintercalated K^+ reached a turning point, the interlayer spacing of K-MnO_2 stopped increasing, and the excessive preintercalated K^+ would produce repulsive interaction with the inserted K^+ to depress its diffusion with D_{K+} decreasing from 8.92×10^{-9} cm^2 s^{-1} ($K_{0.19}MnO_2$) to 6.02×10^{-9} cm^2 s^{-1} ($K_{0.215}MnO_2$) (Figure 8e,f).

Developing MnO_2 materials with greater interlayer spacing can be an effective strategy to resolve the issue of sluggish insertion and diffusion kinetics of the divalent Zn^{2+}/Mg^{2+} ions in MnO_2 host structures. Intercalation of some organic species (e.g., TMA^+, polyaniline) provides an effective method to fabricate outstanding active cathode materials. Wang et al. studied the Mg^{2+} storage ability of layered δ-MnO_2 by altering the original intercalated ions.[45] When the intercalated ions changed from K^+ to TMA^+, the (001) peak showed a 2theta shift from 5.67° to 4.37°, corresponding to an increase of interlayer spacing from 0.70 to 0.97 nm, which enabled easier diffusion of hydrated Mg^{2+} ions (**Figure 9**a,b). Also, the preintercalated TMA^+ ions in layered MnO_2 tends to be stable even after repeated insertion/ extraction of the hydrated Mg^{2+}. As a result, the specific capacities nearly doubled from 58.6 to 110.9 mAh g^{-1}, and the

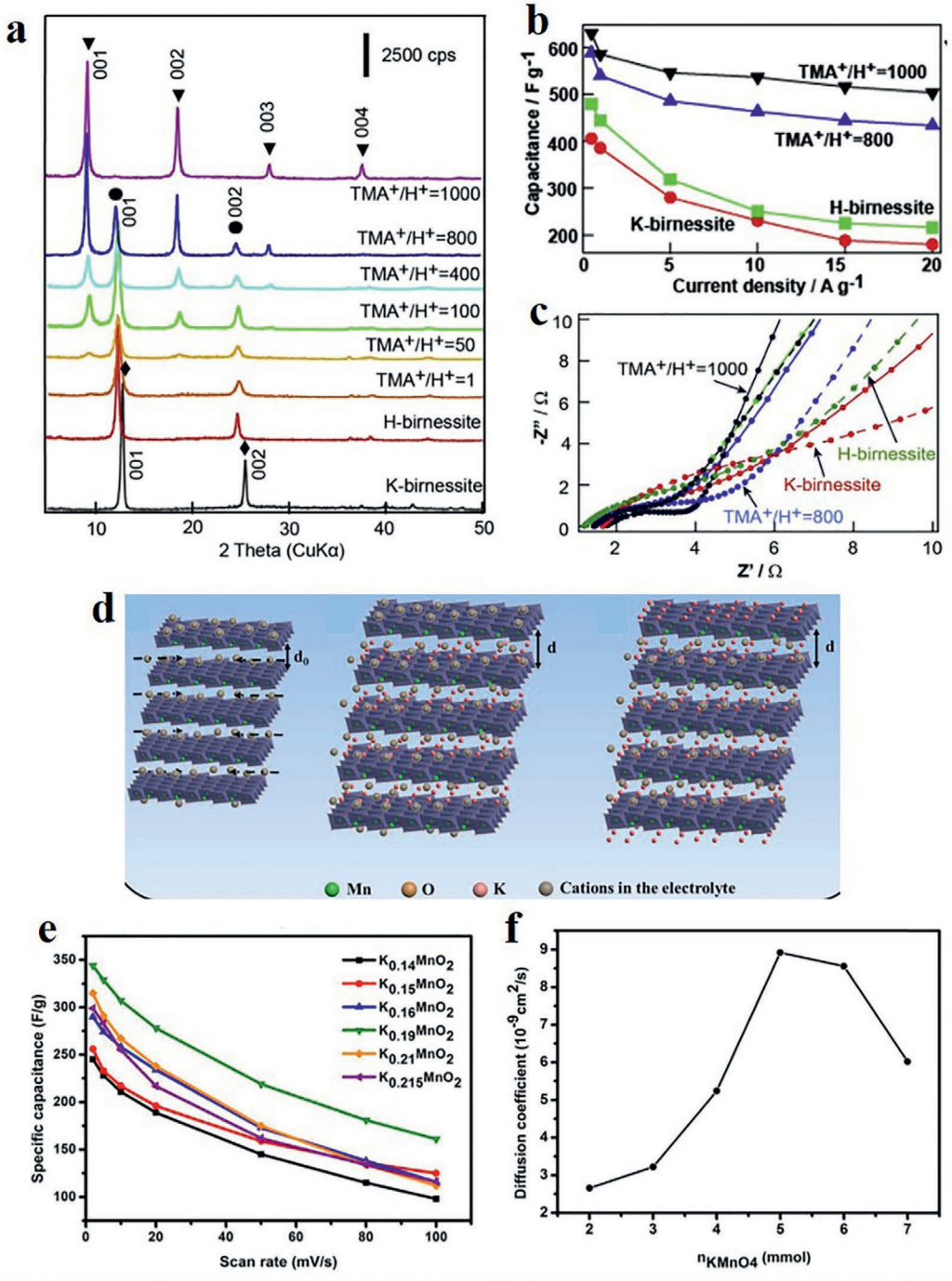

Figure 8. Enhanced diffusion kinetics of monovalent ions in MnO_2 due to the expanded interlayer spacing. a) The diffraction peaks of TMA-δ-MnO_2, H-δ-MnO_2, and K-δ-MnO_2, respectively, b) specific capacitance at different current density, and c) EIS plots before cycling (solid symbols) and after charge/discharge for 10 000 cycles (empty symbols) for different samples. d) Schematic illustration of charge processes of δ-MnO_2, δ-$K_{0.19}MnO_2$, and δ-$K_{0.215}MnO_2$, e) specific capacitance versus scan rate for samples with different amount of preintercalated K^+ ions, and f) diffusion coefficient of K ions in each sample. a–c) Reproduced with permission.[49] Copyright 2017, Elsevier. d–f) Reproduced with permission.[108] Copyright 3027, Elsevier.

rate capability was also significantly improved (Figure 9c,d). In most cases, the preintercalated tetraalkylammonium cations can remain stable in the interlayer of manganese oxides during cycling. However, there also has some exceptions, for instance, Nakayama et al.[109] reported that when cycling in a KCl solution, the preintercalated tetraethylammonium (TEA^+) ions between the Mn oxide layers of birnessite-type MnO_2 are rapidly replaced with K^+ in solution by ion exchange, accompanying a shrinkage of the interlayer.

Xia's group[24] reported the design of a polyaniline-intercalated layered MnO_2 (with an expanded interlayer space of ≈10 Å) to promote the Zn^{2+} diffusion in an aqueous Zn ion battery. Due

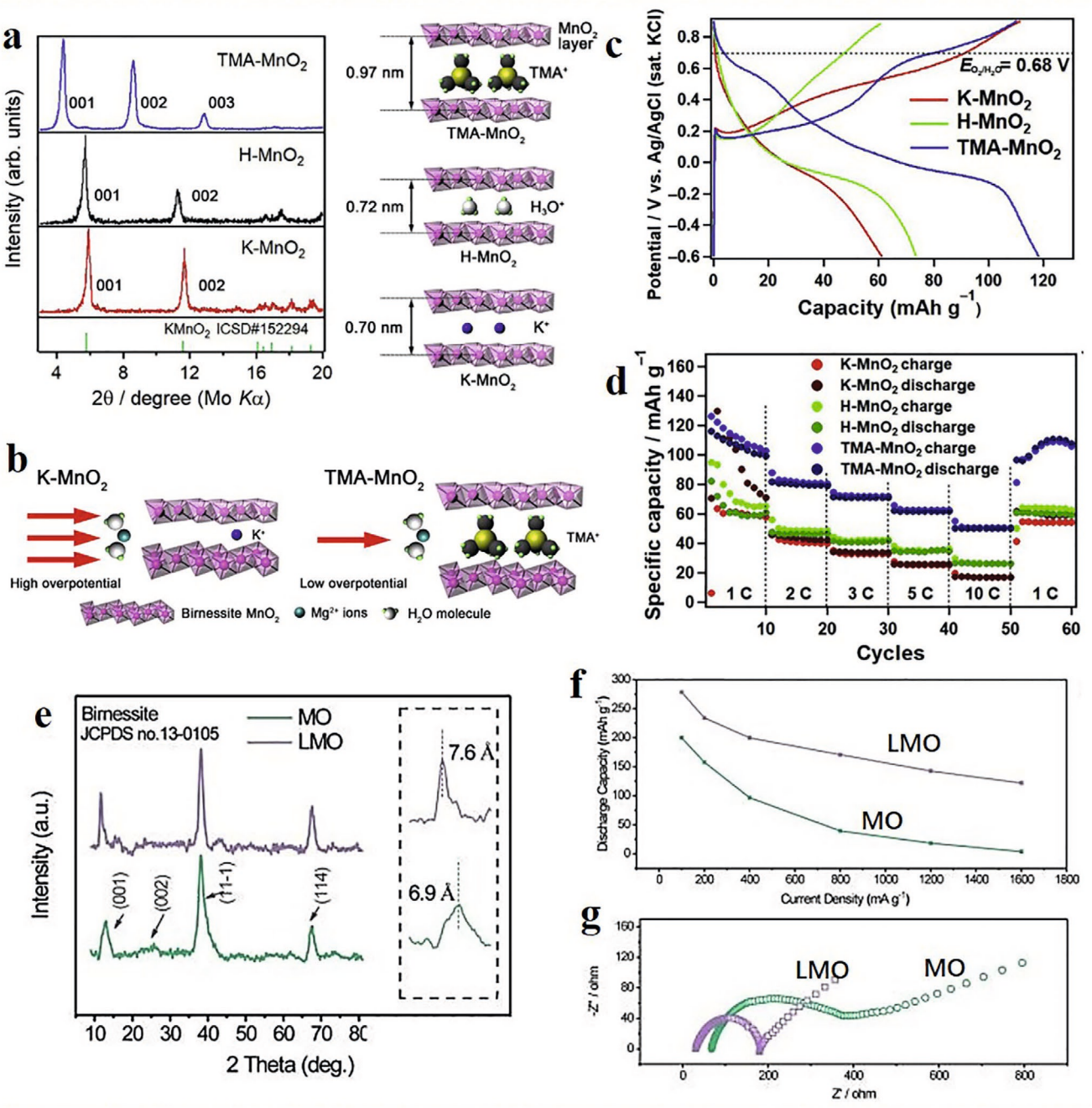

Figure 9. Expanding interlayer spacing of MnO_2 to enhance the diffusion kinetics of Mg^{2+}/Zn^{2+} ions. a) XRD patterns of the synthesized K-MnO_2, H-MnO_2, and TMA-MnO_2 powders; b–d) schematic diagrams of their interlayer spacing (b), capacity delivery (c), and rate performances (d) of the K-MnO_2, H-MnO_2, and TMA-MnO_2 cathodes. e) XRD patterns of δ-MnO_2 (MO) and La^{3+} preintercalated δ-MnO_2 (LMO), and f,g) corresponding rate performances (f) and EIS plots (g) indicating an enhanced diffusion kinetics of Zn^{2+} ions due to La^{3+} preintercalation. a–d) Reproduced with permission.[45] Copyright 2019, Elsevier. e–g) Reproduced with permission.[25] Copyright 2019, Royal Society of Chemistry.

to the polyaniline-intercalated layer-structure, the cathode still could deliver a capacity of 110 mAh g^{-1} even at the high current density of 3000 mA g^{-1}, indicating a high diffusion kinetics of hybrid H^+/Zn^{2+} ions. Lee et al.[103] reported that due to the large 3×3 tunnels, the todorokite-type MnO_2 showed faster Zn^{2+} diffusion as cathode for aqueous Zn-ion batteries, comparing with that of the α-MnO_2 with 2×2 tunnels. Zhang et al.[110] reported a facile phosphorization process for introducing oxygen defects into phosphate ions intercalated δ-MnO_2 (P-MnO_x) as cathode for aqueous Zn-ion batteries, in which the oxygen defects could increase the electronic conductivity of δ-MnO_2, and the intercalated phosphate ions was able to expand the interlayer spacing to accelerate the diffusion of H^+/Zn^{2+}. Due to the increased electronic conductivity and enlarged interlayer spacing, the

phosphate preintercalated δ-MnO_2 demonstrated the greatly reduced Warburg resistance and promoted ionic diffusion comparing with that of the pristine δ-MnO_2. The P-MnO_x showed a high rate performance of 151 mAh g^{-1} at 10 A g^{-1} (≈30 C), which was much higher than that of pure δ-MnO_2. Furthermore, Lu's group[25] revealed that the layer thickness of La^{3+} preintercalated δ-MnO_2 (La-δ-MnO_2) calculated from the angle value of (001) plane increased from 6.9 Å to 7.6 Å (Figure 9e), mainly due to the introduction of La^{3+}, which reduced the resistance of Zn^{2+} (de)insertion, then further improved the Zn^{2+} diffusion kinetics and storage ability. Thus, the La-δ-MnO_2 cathode showed more superior rate performance with a remarkable capacity retention of 121.8 mAh g^{-1} at 1600 mA g^{-1}, comparing with the ultralow capacity retention of 3.4 mAh g^{-1} at 1600 mA g^{-1} for the pristine δ-MnO_2 (Figure 9f,g).

In summary, in this section, we conclude two effective preintercalation strategies to promote the intrinsic diffusion kinetics of MnO_2 materials, i.e., reducing effective charge of carrier ions via charge shielding effect of crystal water, and expanding interlayer spacing to decrease the electrostatic repulsion between carrier ions and host framework of MnO_2 materials. The charge shielding effect of crystal water is mainly attributed to the hydrogen-bonding-like interaction between crystal water and carrier ions, as identified by several DFT calculations. This charge shielding effect of crystal water is vital for the feasible storage and transport of carrier ions in MnO_2 cathodes, e.g., Li^+, Na^+, Zn^{2+}, Mg^{2+}, etc. With crystal water inside MnO_2 materials, the migration barrier of Zn^{2+}/Mg^{2+} ions are much lower than that of the MnO_2 without crystal water. In addition to charge shielding effect of crystal water, expanding interlayer spacing or tunnel size of MnO_2 materials via preintercalation is another effective method to facilitate diffusion kinetics. Especially, with preintercalated large ions/ molecules (e.g., TMA^+, polyaniline), the interlayer spacing of layered MnO_2 can be greatly expanded, which will benefit for the diffusion of multivalent carrier ions (e.g., Zn^{2+}, Mg^{2+}). Besides, there exists an optimum content of intercalated species in MnO_2 materials to achieve the best electrochemical performance. In the end, in many cases, both the charge shielding effect of crystal water and expanding interlayer spacing works together to promote the diffusion kinetics of carrier ions, and realize an excellent rate performance of MnO_2 electrodes.

6. Stabilizing Structure Integrity

Structural instability (including dissolution of $Mn^{3+/2+}$, and phase transition) was generally considered as the main reason for the capacity fading issue of MnO_2-based cathodes in various battery applications, including lithium ion batteries,[111,112] mild aqueous M-ion batteries (M = Li,[113] Na,[114] Mg,[97] and Zn,[115] etc.), alkaline Zn batteries,[116,117] and so on. This structural instability is mainly induced by the formation of Mn^{3+} ions with the insertion of carrier ions into the tunnels/ interlayers of MnO_2 materials. It is well known that the Mn^{3+} ion was unstable due to its high spin d^4 (= t_{2g}^3-e_g^1) electronic configuration in octahedral symmetry.[118,119] Furtherly, according to Shannon's table, the Mn^{4+}—O bond length (1.93 Å) was predicted to elongate when the Mn was reduced to Mn^{3+} (2.045 Å) or Mn^{2+} (2.23 Å),[120] which resulted in the weakened Mn—O bonding strength, and the increased disorder degree of the lattice arrangement, i.e., Jahn–Teller (J–T) effect. Additionally, the intercalated carrier ions exhibited electrostatic repulsion and physical extrusion interactions on reduced [$Mn^{3+}O_6$] octahedrons or [$Mn^{2+}O_4$] tetrahedrons. As a result, the [$Mn^{3+}O_6$] octahedrons/ [$Mn^{2+}O_4$] tetrahedrons could be easily squeezed out from the crystal lattice of MnO_2 hosts (including both the tunnel-type and layer-type MnO_2) after insertion of carrier ions, and then the dissolution of $Mn^{3+/2+}$ or/and the phase transition occurred.

The above mentioned structural instability of MnO_2 induced by the J–T effect led to the large and anisotropic volumetric change, undermined the structural integrity, and blocked the ion diffusion pathways, and thus resulted in the capacity fading of MnO_2.[121,122] In this section, we focus on the preintercalation effect on stabilizing the structure integrity of MnO_2 during charge/discharge process. To distinguish the difference of capacity fading issues induced by the dissolution of $Mn^{3+/2+}$ ions and the phase transitions, herein, by reviewing the literatures, we proposed a basic and fundamental hypothesis, i.e., the dissolution of $Mn^{3+/2+}$ is usually observed on the electrolyte/electrode interface for MnO_2 cathodes, or in the interlayer region of δ-MnO_2 with large layer spacing, while the phase transition processes occurs in the overall MnO_2 particles. It should also be noted that the dissolution of Mn^{3+} was very special, and was only observed in alkaline batteries in the form of soluble intermediate of $[Mn(OH)_6]^{3-}$.[117] Furtherly, for some δ-MnO_2 with interlayer spacing larger than 10 Å, the Mn^{2+} ions could escape from the [MnO_6] layers upon discharge, and formed an octahedral $[Mn(H_2O)_6]^{2+}$ in the interlayer region,[31] which could migrate into the electrolyte, and was regarded as a special dissolution type of Mn^{2+}. Besides, we also notice that the degree of structure instability and Mn dissolution of the MnO_2 with different structures (tunnel-type α-, β-, and γ-, and layer-type δ-MnO_2, etc.) is different. Comparing with layer-type MnO_2, the tunnel-type MnO_2 usually present 1D diffusion paths, which makes the crystal structure distortion easier to occur during charge/discharge processes, and then leads to more serious problems of structure instability and Mn dissolution.

6.1. Reducing Mn^{2+} Dissolution of Manganese Oxides via Preintercalation

For MnO_2 materials, the Mn^{2+} dissolution from MnO_2 due to J–T effect led to the decreased quality of active materials.[61] In general, Mn^{2+} dissolution for MnO_2 is affected by various conditions, such as crystal structure, carrier ion species, state of charge/discharge, etc. To alleviate capacity fading induced by the Mn^{2+} dissolution, various treatments were proposed, such as surface coating,[123,124] metal doping,[125,126] tuning crystalline orientations,[111] preaddition of Mn^{2+} in electrolyte,[127] and preintercalation,[51,128] etc., however, it has so far not completely eliminated. The preintercalation of crystal water, ions, or organic species are effective strategies to reduce the Mn^{2+} dissolution. Fang et al.[128] reported that the Mn^{2+} dissolution could be suppressed via preintercalated K^+ ions in α-MnO_2. It could be seen that the dissolution of Mn^{2+} could be effectively alleviated in K^+-α-MnO_2 even after 50 cycles, while the α-MnO_2 exhibited a fast dissolution of Mn^{2+} during cycling (**Figure 10**a), which led to impedance rise and capacity fading. The results showed that it was possible to suppress the Mn dissolution as

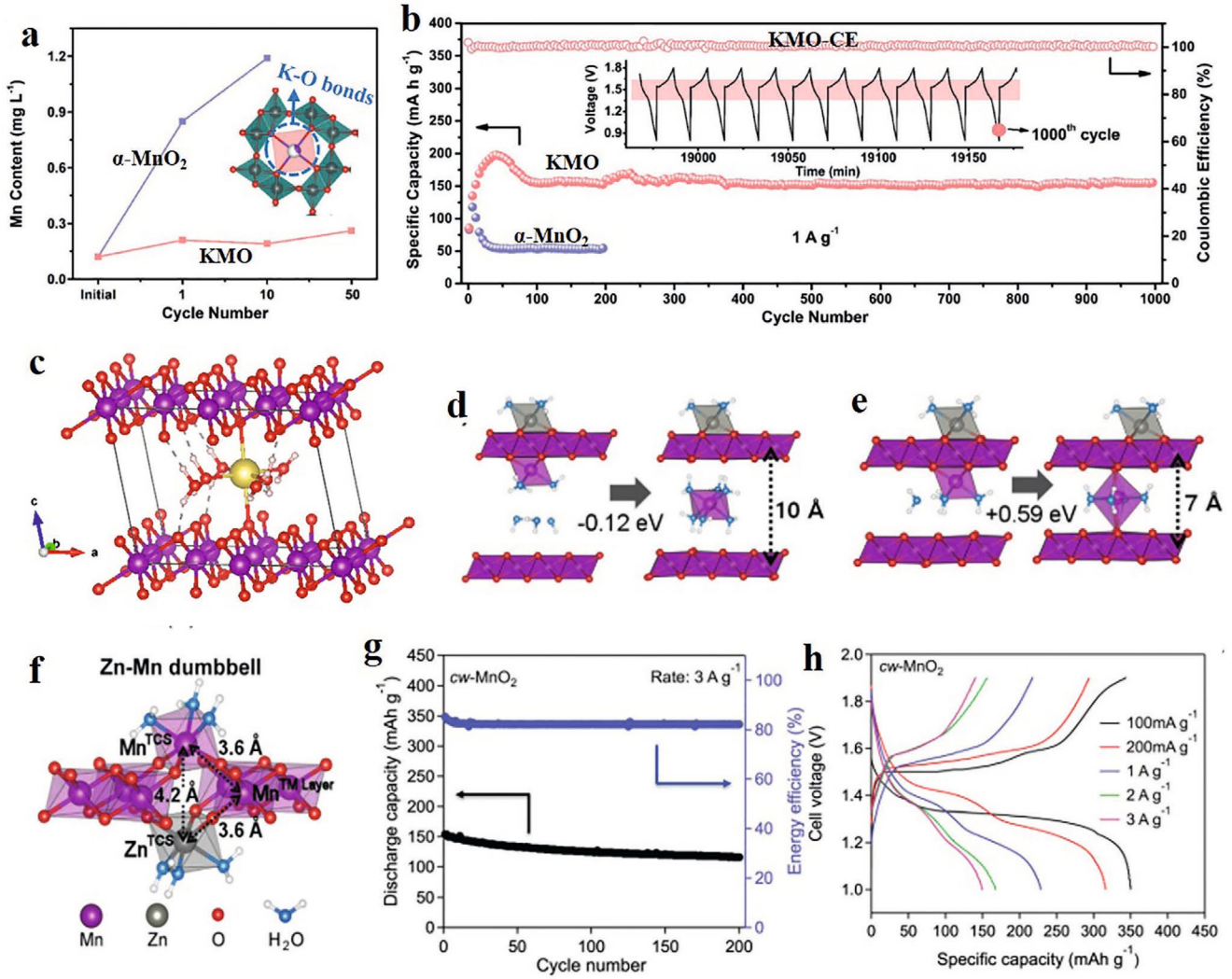

Figure 10. Depression effect of preintercalation on Mn^{2+} dissolution of MnO_2. a) Element analysis of dissolved Mn^{2+} in a 2 M $ZnSO_4$ aqueous electrolyte during cycling of KMO and α-MnO_2, b) long-life cycling performance of KMO and α-MnO_2 electrodes at 1000 mA g^{-1}. c) Local Na^+ environment in Na-birnessite. d,e) The energetically distinct complexation behavior of Mn-octahedrons with different interlayer distances: d) 10 Å and e) 7 Å. f) The inner-sphere complexation of Zn induces the protrusion of the facing Mn, constituting a Zn–Mn dumbbell structure, and g,h) the corresponding cycling (g) and rate performances (h) of cw-MnO_2 materials. a,b) Reproduced with permission.[128] Copyright 2019, Wiley-VCH. d–h) Reproduced with permission.[99] Copyright 2019, Royal Society of Chemistry.

the K^+ ions steadily intercalated into the tunnels of K^+-α-MnO_2 and bonded with the Mn polyhedrons, thus strengthening its inherent stability (Figure 10b). As a result, the K^+ pre-intercalated α-MnO_2 obtained an impressive durability over 1000 cycles with no obvious capacity fading.

Docheon et al.[129] reported that the intercalated Co^{2+} in interlayer of δ-MnO_2 could supply sufficient structural stability during cycles due to their depressing effect on Mn^{2+} dissolution. The layered $K_{0.08}Co_{0.12}MnO_2$ was synthesized by exchanging 75% of the K^+ ions in the pristine K-birnessite ($K_{0.32}MnO_2$) with Co^{2+} ions through an ion-exchange reaction at room temperature. Since the intercalated Co^{2+} ions with small radii were usually located above and below each MnO_6 octahedral vacancy, they acted as pillars and hinder the diffusion of Mn^{2+} ions into the interlayer region, and thus effectively prohibited the structural conversion during cycles. Thus, $K_{0.08}Co_{0.12}MnO_2$ showed excellent cyclability over 40 cycles for Li^+ ion storage.

Li et al.[107] revealed that the crystal water in Na-birnessite might depress the Mn^{2+} dissolution, remit the lattice transformation caused by the J–T effect, and thus enhanced the structural stability as well as the prolonged the cycling stability of Na-birnessite. Similarly, Nam et al.[49] reported the depressed Mn^{2+} dissolution in $Na_{0.4}MnO_2 \cdot 0.25H_2O$ cathode, due to the existence of crystal water. They considered that the insertion/extraction of the large-size Na^+ could generate great strain in the neighboring MnO_6 layers, which led to large volumetric change, and an accelerated Mn^{2+} dissolution from the layers. The pre-intercalated crystal water could suppress the dissolution of Mn^{2+} by serving as interlayer pillars based on hydrogen bonding with MnO_6 layers, and thus maintained the intermediate and long-range stacking of Mn–O octahedral layers well.[130] It was reported that the hydrogen bonding between crystal water and [MnO_6] layers could hold the layers together, and the Na^+ was fully hydrated within the birnessite framework which showed

no direct interaction with the [MnO_6] layers (Figure 10c).[131] Thus, owing to this special hydrogen bonding between crystal water and [MnO_6] layers, the strain induced by shuttling of Na^+ ions was lowered, which effectively depressed the Mn dissolution and prolonged the cycle life of δ-MnO_2 cathodes.

In 2019, Nam et al.[99] also reported that the appropriate interlayer distance and high water content could jointly contribute to sustainable cycling by alleviating Mn dissolution and stabilizing the host framework during cycling. They found that when the interlayer distance of buserite MnO_2 was larger than 10 Å, the Mn^{2+} ions could escape from the [MnO_6] layers upon Zn^{2+} insertion, leading to the formation of an octahedral $[Mn(H_2O)_6]^{2+}$ complex even inside the crystal structure, then the $[Mn(H_2O)_6]^{2+}$ could migrate into the electrolyte, which was the origin of capacity fading in the α-and β-MnO_2 electrodes that transformed to a buserite during cycling with a large interlayer spacing of ≈11 Å (Figure 10d). While for the cw-MnO_2 with interlayer spacing of ≈7 Å, the mobility of Mn^{2+} ions were limited in the birnessite structure due to the insufficient interlayer distance for Mn^{2+} dissolution, thus the Mn^{2+} dissolution was depressed. Furthermore, they also revealed that the $[Mn(H_2O)_6]^{2+}$ centered in the interlayer space was unstable by 0.59 eV, and tended to form a Zn–Mn dumbbell configuration (Figure 10e,f). The formation of this Zn–Mn dumbbell superstructure not only benefited for depressing Mn^{2+} dissolution to achieve high cycling performance, but also accelerated the charge transfer process to obtain higher capacity and rate properties. As a result, the cw-MnO_2 electrode also showed decent cycling stability with capacity retention of 75.3% after 200 cycles at current density of 3000 mA g^{-1} (Figure 10g), a high reversible capacity of 350 mA h g^{-1} at 100 mA g^{-1}, as well as excellent rate performance with 154 mA h g^{-1} at 3000 mA g^{-1} (Figure 10h).

6.2. Origin of Phase Transition of Tunneled/Layered MnO_2

To reveal the preintercalation effect in depressing the phase transformation of manganese oxide, we first explore the origin of phase transition of MnO_2 materials with tunneled/layered structures. The inevitable phase transition has been extensively reported in lots of battery applications. For example, in aqueous Zn ion batteries, the phase transition from tunnel to layer structures were reported for α-, β-, and γ-MnO_2,[31,132,133] the layered δ-MnO_2 was reported transforming to spinel Mn_3O_4 and $ZnMn_2O_4$,[54] and the spinel Mn_3O_4 could transform to intermediate Mn_5O_8 and finally to Zn-birnessite during discharge process.[134] Similarly, the phase transformation also existed in MnO_2 cathodes for insertion/ extraction of H^+, Na^+, and Mg^{2+} ions,[13,135,136] indicating the universality of phase transition phenomenon during charge/ discharge processes of MnO_2. This phase transformation demonstrated that the crystal structure of MnO_2 was unstable during insertion/ extraction process of carrier ions. Notably, the formation of some inactive phases (e.g., Mn_3O_4 and $ZnMn_2O_4$) contributed to the capacity fading of MnO_2.[15,116]

The above-mentioned phase transformation is attributed to the structural distortion during insertion/extraction of carrier ions. For tunneled α-MnO_2, the typical distortion form was the strong tetragonal to orthorhombic (T–O) distortion during discharge process, which might destruct the integrity of the host framework. This kind of T–O distortion has been reported in various batteries with α-MnO_2 cathodes, including Li-ion,[67,112,113] Na-ion,[12,137] Zn-ion,[127,138,139] and Mg-ion batteries.[140] For example, Alfaruqi et al.[138] revealed that the unit cell volume of the [2 × 2] tunnels in the α-MnO_2 host expanded by ≈3.12% during Zn-insertion. Chen et al. reported that the quasi-square tunnel of α-MnO_2 host deformed greatly after Mg-insertion,[140] with joint angle (θ) between corner shared [MnO_6] octahedrons changing from 98.3° to 73.3°, which damaged the structural stability of the discharged α-MnO_2. Therefore, the T–O distortion occurred upon the insertion process, and when the degree of disorder reached a critical point, the host structure would undergo phase transformation to form the layer/spinel phases, and consequently the structure collapse of layered structure arose during cycling.

The phase transformation from layered to spinel structure was induced by the rearrangement of Mn-ions and inserted carrier ions, which has also been observed in various batteries, such as Li-ion,[69,141] Na-ion,[135,142–146] Zn-ion,[115,147,148] Ca-ion,[149] and Mg-ion batteries.[13,98] For example, Lim et al.[141] revealed that the thermodynamically stable structures were determined along a decreasing Li content: a monoclinic structure (x = 0–0.75), layer-like structure (x = 1.0–1.25), and spinel-like structure (x = 1.5–2.0). Alfaruqi et al.[52] proposed structural variation of δ-MnO_2 in aqueous Zn batteries, i.e., the layered structure of δ-MnO_2 was transformed gradually into a spinel phase upon multiple charge/discharge cycles. Sun et al.[13] also revealed a "layer to spinel" phase transformation in a Mg ion battery. After Mg^{2+} insertion into the layered MnO_2, the structure of the discharged phase presented the same layer arrangement as spinel phase; i.e., Jahn–Teller distorted, partially occupied triangular slabs interconnected by tetrahedral MgO_4 and octahedral MnO_6 cells. However, the stacking scheme of this discharged phase did not exactly reproduce the 3D structure of $MgMn_2O_4$. In summary, the phase transition from layer to spinel structure was inevitable, accompanying with subsequent increased structural disorder, structure collapses, as well as the blocked ion transport channels in layered MnO_2, then the capacity fading appeared.

6.3. Stabilizing Effect of Preintercalation Strategy on Structure of Tunneled MnO_2

For α-MnO_2, Mn ions were in mixed valence states (Mn^{3+} and Mn^{4+}), where charge neutrality was maintained by cations residing in tunnels. The most common form was K^+ intercalated α-MnO_2,[22] however, the [2 × 2] tunnels of α-MnO_2 could also be hosts for H_2O and various other cations such as H_3O^+, Li^+, Na^+, Ag^+, Zn^{2+}, Mg^{2+} ions.[150,151] The crystallinity and thermal stabilities of MnO_2 materials were affected by the nature of the ions and the amount of structural water.[152] Larger ions led to better crystallinity and a more ordered tunnel structure with high thermal stability, while more tunnel water reduced the order of the tunnel-type structure resulting in lower thermal stability. On the one hand, the residing ions inhibit the collapse of the tunnels to promote insertion of carrier ions,[153] on the other hand, these residing ions can interact with the carrier ions (Li^+, Na^+, Mg^{2+}, etc.), and impede the insertion by physical blocking and repulsive electrostatic forces.[154] Thus, the

preintercalation strategy effect on cycling performance of MnO_2 cathodes remains controversial for the tunnel-type α-MnO_2.

Poyraz et al. revealed the role of tunnel K^+ ions in the Li-ion electrochemistry of α-MnO_2 materials in the nonaqueous cells.[67] The α-MnO_2 materials had a chemical composition of $K_xMn_8O_{16}\cdot yH_2O$, where $0 < x < 0.75$ and $0.53 < y < 0.81$. They suggested that although the K^+ in the tunnels could stabilize the structure of α-MnO_2, it impeded the Li^+ diffusion, thus the K^+ content in $K_xMn_8O_{16}\cdot yH_2O$ ($x < 0.32$) should be lower to achieve higher specific capacity and high cycling performance. Furthermore, with increasing K^+ in the tunnels, an increase in Mn–Mn wall distortion was observed at high levels of lithiation, as indicated through EXAFS modelling (**Figure 11**a), resulting in the decreased capacity retention for $K_xMn_8O_{16}\cdot yH_2O$ samples with increasing K+ content (Figure 11b). The above discussions indicate that in some circumstance, the preintercalation strategy may play a bad effect on the cycling performance. Another opinion considered that the preintercalation strategy benefited to the cycling performance of MnO_2 cathodes. For example, Fang et al.[128] reported the stabilizing effect of K^+ ions on cycling performance of α-MnO_2. Further, to eliminate the blocking effect of K^+ ions on diffusion of H^+/Zn^{2+}, the authors also introduced oxygen vacancy to increase the diffusion kinetics via gaining more ion diffusion pathways (Figure 11c). As a result, the K^+ preintercalated MnO_2 (KMO) possessed impressive durability over 1000 cycles at 1000 mA g^{-1}, and the last ten charge/discharge curves of KMO electrode at 1000 mA g^{-1} remain almost the same with a satisfactory operating voltage (over 1.35 V), further demonstrating the high stability and reversibility of KMO electrode. Besides, it was also reported that ions with larger size would benefit more for enhancing structural stability of α-MnO_2. Huang et al. investigated the Ag^+ and K^+ stabilized α-MnO_2 materials as high voltage cathode materials for Mg-ion batteries,[151] and revealed that the cycling stability of K^+-α-MnO_2 electrode was higher than that of Ag^+-α-MnO_2 electrode, mainly due to the larger ionic radius radii of K^+ (1.38 Å) compared to that of Ag^+ (1.15 Å) and the stabilizing effect of the K^+ ion in the tunnels (Figure 11d).

It has also been accepted that the structural water in tunnels of MnO_2 could reduce the volume expansion upon ion insertion. Frey et al.[52] revealed this reducing effect of structural water on the volume expansion upon insertion of sodium ions. Between the unit cell with structural Na^+ ions from $x_{Na} = 0.2$ to $x_{Na} = 0.4$, there was a ≈3.4% volume increase from ≈189.9 $Å^3$

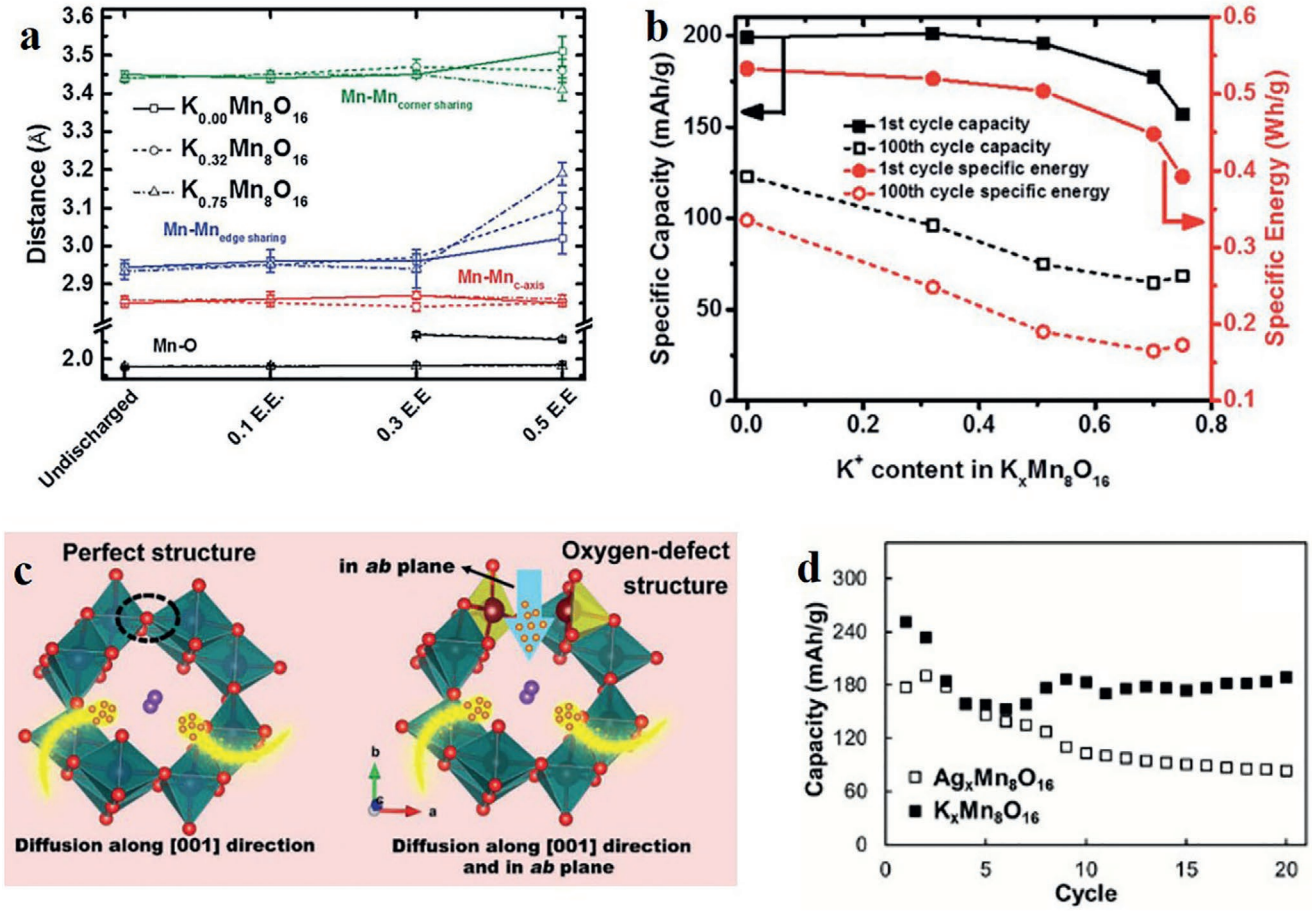

Figure 11. Structural distortion of α-MnO_2 during discharge. a) EXAFS interatomic distance modeling results for α-MnO_2 with different K^+ contents at 0 (undischarged), 0.1, 0.3, and 0.5 lithiation levels, and b) evolution of specific capacity and energy at 1st and 100th cycle with different K^+ contents of $K_xMn_8O_{16}$ samples. c) Schematic comparison of H^+ diffusion into K^+-stabilized α-MnO_2 with perfect structure and oxygen-defect structure. d) Cycling performance of $Ag_xMn_8O_{16}$ and $K_xMn_8O_{16}$ samples at 50 mA g^{-1}. a,b) Reproduced with permission.[67] Copyright 2017, Royal Society of Chemistry. c) Reproduced with permission.[128] Copyright 2019, Wiley-VCH. d) Reproduced with permission.[151] Copyright 2016, Royal Society of Chemistry.

to ≈196.4 Å^3 without structural water. However, with structural water, this volume change due to insertion was ≈1.7%, from ≈199.2 Å^3 to ≈202.6 Å^3. Thus, by reducing volume expansion upon insertion, the structural water in tunnels of MnO_2 might be expected to improve the cycling stability. In fact, for most tunneled MnO_2, the coexistence of preintercalated ions and crystal water played a synergistic role on improving the structural stability during charge/ discharge cycles.

6.4. Stabilizing Effect of Preintercalation Strategy on Structure of Layered MnO_2

For the layered MnO_2 materials, the crystal structure could be highly distorted, disordered or even destructed, and then transform to inactive spinel-type materials upon cycling, which leads to poor cycling stability. To inhibit the formation of inactive spinel phase, preintercalation strategy is needed. For layered δ-MnO_2, the preintercalation of ions or molecules could be an effective strategy to depress the phase transition induced capacity fading issues. The ions/ molecules preintercalated in layered δ-MnO_2 should satisfy the following conditions: i) the preintercalated ions/ molecules are not easily extracted from the host during charging process; ii) the interlayer spacing should be lower than ≈11 Å, for which can limit the formation of $[Mn(OH)_4]^{2-}$ inside the interlayer of MnO_2, and the subsequent migration into electrolyte; iii) the preintercalation of ions must be accompanied with certain amount of crystal water, due to its charge-shielding effect to reduce the electrostatic repulsion between the preintercalated ions and the carrier ions.

By reviewing literatures, we propose that by preintercalating cations, such as K^+,[90] Rb^+,[38] Cu^{2+},[155] Zn^{2+},[156] and La^{3+}ions,[25] the phase transition from layer to spinel can be depressed due to the reduced volumetric change during charge/discharge process, and thus alleviating the capacity fading of MnO_2 cathode. For example, Liu et al.[23] also reported that the high content preintercalated K^+ ions into the layered-type matrix as pillars stabilize the layered structures

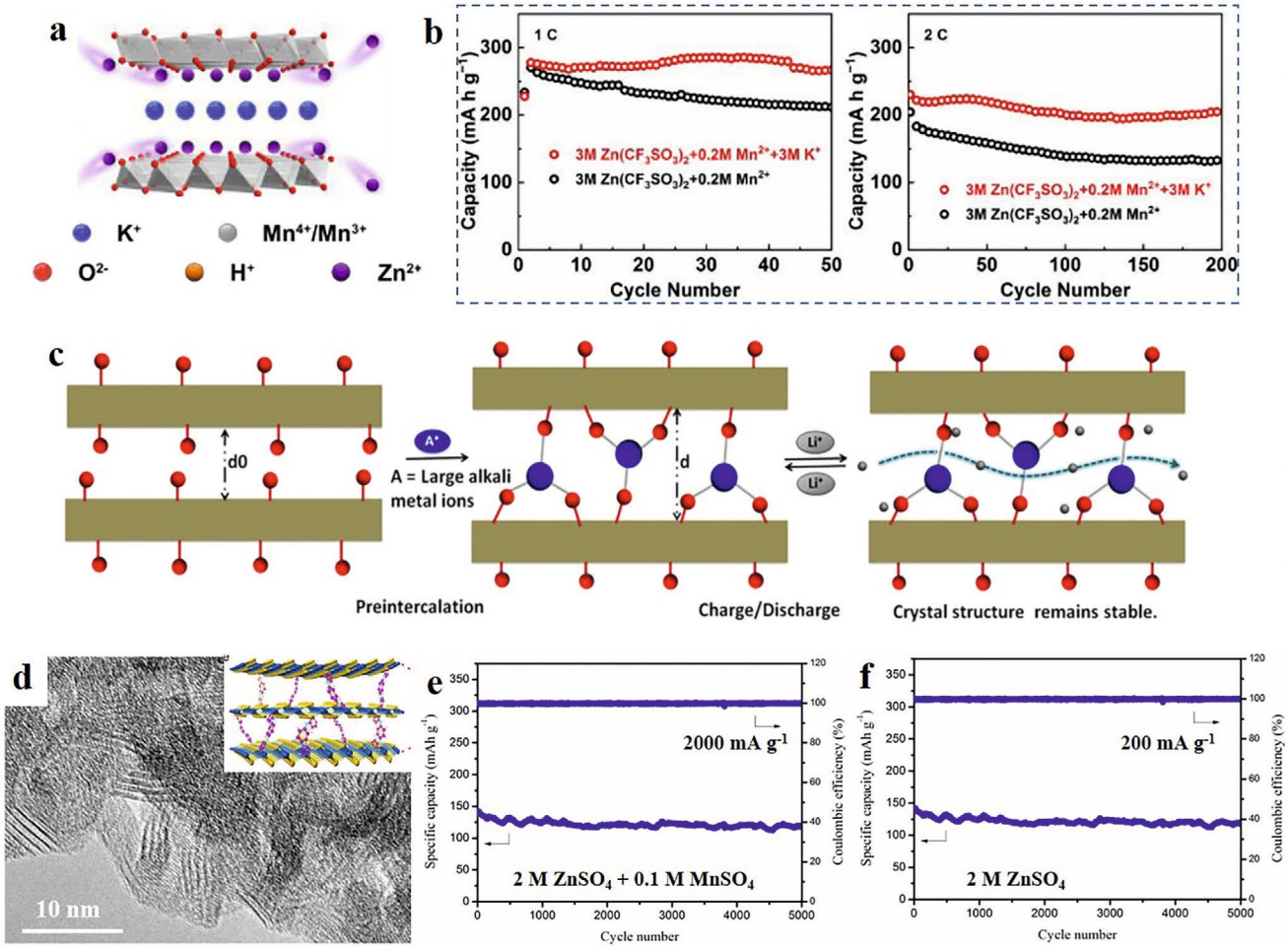

Figure 12. Preintercalation of ions/molecules in layered MnO_2 to depress phase transformation. a) Schematic illustration of H^+/Zn^{2+} insertion/extraction in K^+-stabilized δ-MnO_2, and b) addition of K^+ into the electrolyte to further enhance the cycling stability of K^+-stabilized δ-MnO_2 electrode. c) Schematic illustration of large alkali-metal-ion preintercalation. d) TEM morphology of polyaniline-intercalated MnO_2, and e,f) cycling performance of corresponding electrode in 2 M $ZnSO_4$ + 0.1 M $MnSO_4$ (e) and 2 M $ZnSO_4$ (f). a,b) Reproduced with permission.[23] Copyright 2019, Royal Society of Chemistry. c) Reproduced with permission.[38] Copyright 2015, American Chemical Society. d–f) Reproduced under the terms of the CC-BY Creative Commons Attribution 4.0 International license (https://creativecommons.org/licenses/by/4.0).[24] Copyright 2018, The Authors, published by Springer Nature.

and expand Zn^{2+} migration channels, which can facilitate the diffusion of Zn^{2+} in the MnO_2 cathodes and increase the crystal stability of the layered MnO_2 (**Figure 12**a). Notably, they also employed a K-salt additive in electrolyte to inhibit the extraction of K^+ from the $K_{0.19}MnO_2$ with aim to maintain to host material during cycling, thus, the cycling ability is furtherly boosted (Figure 12b). Zhao et al.[38] revealed that preintercalation with some ions, A–M–O compounds (A = K, Rb; M = V, Mo, Co, Mn) yields a more stable interlayer expansion, which prevents destructive collapse of layers and allow Li^+ ions to diffuse more freely (Figure 12c). As a result, the cycling stability of the electrodes is greatly enhanced. Jiang et al.[154] investigated the Cu^{2+} ions inserted into the interlayer of δ-MnO_2 as cathode in an alkaline battery with KOH solution, and reported that the Cu^{2+} ions have effects to inhibit the irreversible phase transformation into the inactive Mn_3O_4 phase, and thus maintain electrochemical activity under the basic condition. As inspired by the result conducted by Nasar's group,[100] in which they proposed the preintercalated Zn^{2+} and water pillars into V_2O_5 interlayers to stabilize the structure and cause ion migration for high-capacity and long-life ZIBs, Wang et al.[156] reported a δ-MnO_2 stabilized by hydrated Zn^{2+} pillars as cathode for aqueous Zn batteries. The preintercalated hydrothermal Zn^{2+} pillars not only avoided phase reorganization but also enabled a robust structure and better reaction kinetics. However, the authors did not provide a specific explanation for how the preintercalated Zn^{2+} and H_2O inhibit the formation of inactive phases. Zhang et al.[25] reported a birnessite δ-MnO_2 with preintercalated La^{3+} ion as cathode for aqueous Zn ion battery. After introducing La^{3+} into the interlayer of δ-MnO_2, the interlayer spacing increased from 6.9 to 7.6 Å, which was responsible for the enhanced structural stability via decreasing electrostatic and physical interaction between the inserted Zn^{2+} and [MnO_6] layers. Thus, the La^{3+} intercalated δ-MnO_2 displayed excellent cycling performance with capacity retention of 71.0% after 200 cycles, which is much higher than that of the δ-MnO_2. Also, Huang et al.[24] reported a polyaniline-intercalated layered manganese dioxide to improve the cyclability of layered MnO_2 as cathode for aqueous Zn-ion battery. The polyaniline-strengthened layered structure and nanoscale size of MnO_2 materials eliminated the phase changes successfully (Figure 12d), and successfully promote the cycling performance with a long-term cycle life over 5000 cycles at 2000 mA g^{-1} in $ZnSO_4$ + $MnSO_4$ electrolyte (Figure 12e). Even in $ZnSO_4$ electrolyte without $MnSO_4$, the cycling performance of this polyaniline-intercalated MnO_2 can still operate well (Figure 12f), indicating a dramatically enhanced structure stability due to the polyaniline preintercalation.

What is noteworthy is that sole crystal water cannot well depress the phase transformation of MnO_2 materials. As discussed above, the crystal water could well buffer the electrostatic interactions and volumetric changes in charge/discharge process of layered/ tunnel MnO_2, however, we also observed that solo crystal water was incompetent to depress the phase transition induced capacity fading of MnO_2, and it had to cooperate with other preintercalated ions, such as K^+, Rb^+, etc. For instance, Sun et al.[13] provided the electrochemistry and structural changes of layered MnO_2 as cathode material in an aqueous Mg-ion battery. When cycled in aqueous cells, the insertion of Mg^{2+} ions caused the expulsion of interlayer and transformation to a spinel-like phase. Similar results were also provided by Nam et al.[99] and Alfaruqi et al.[54] in aqueous Zn-ion batteries, which indicated that the formation of an ancillary spinel phases, such as $ZnMn_2O_4$, $MgMn_2O_4$, Mn_3O_4, etc., could not be completely avoided by sole preintercalation of crystal water.

However, it should also be mentioned that the coinsertion of hydrated water and carrier ions could stabilize the layered structure of MnO_2 to some extent. For instance, Shan et al.[145] investigated the electrochemistry of a sodium preintercalated birnessite ($Na_{0.27}MnO_2$ nH_2O) as cathode for aqueous Na-ion batteries. **Figure 13** presented the water trafficking process along with Na-ion's insertion/ extraction during the charge/ discharge process. Notably, the d_{001} decreased from 7.33 to 7.30 Å as the high potential region from 0.914 to 1.25 V, indicating a decrease of interlayer spacing due to the removal of structural water along with Na^+ extraction. This coextraction of the hydrated water and Na-ions during the high potential charging process resulted in the slight shrinkage of interlayer distance, reduced the volumetric change of crystal structure during cycles, and thus stabilized the layered structure of $Na_{0.27}MnO_2 \cdot nH_2O$ compound. Thus, the $Na_{0.27}MnO_2$ nH_2O showed a much-enhanced capacity and cycling life (83 mAh g^{-1} after 5000 cycles in full-cell) for aqueous sodium-ion electrochemical storage.

In summary, the structural instability, including dissolution of $Mn^{2+/3+}$ and phase transition, is the main reason for the capacity fading issue of MnO_2 cathodes in various battery applications. A basic fundamental hypothesis is proposed, that is, the dissolution of $Mn^{3+/2+}$ is mainly appears on the electrolyte/electrode interface for MnO_2 cathodes, or in the interlayer region of δ-MnO_2 with large layer spacing, while the phase transition occurs in the overall MnO_2 particles. The role of preintercalation on depressing the dissolution of $Mn^{3+/2+}$ during cycling is as following aspects: i) the preintercalated ions are located above and below each MnO_6 octahedral vacancies, which serves as pillars and hinders the diffusion of Mn^{2+} into interlayer regions of MnO_2 cathodes; ii) crystal water can suppress the dissolution of Mn^{2+} by serving as interlayer pillars based on hydrogen bonding with MnO_6 layers; iii) the interlayer distance and water content in δ-MnO_2 need to be tuned to effectively alleviating Mn dissolution; iv) the preintercalated ions can be bonded with the Mn polyhedrons to strengthen the inherent stability of α-MnO_2 and suppress the Mn dissolution. The phase transformation is originated from the structural distortion during insertion/extraction of the carrier ions, i.e., the tetragonal to orthorhombic (T–O) distortion for α-MnO_2, a contraction of the interlayer spacing, as well as a glide of the MnO_2 planes for δ-MnO_2. When this structural distortion reaches a turning point, the phase transformation occurs, and some inactive phases form after several decades of cycles. The preintercalation can stabilize the phase structure of MnO_2 materials in the following way: i) the preintercalated ions lead to a better crystallinity and a more ordered tunnel structure with higher thermal stability of α-MnO_2; ii) the structural water in tunnels of α-MnO_2 can reduce the volume expansion upon ion insertion; iii) the preintercalated ions yields a more stable interlayer expansion, which prevents destructive collapse of layers during insertion/extraction processes of

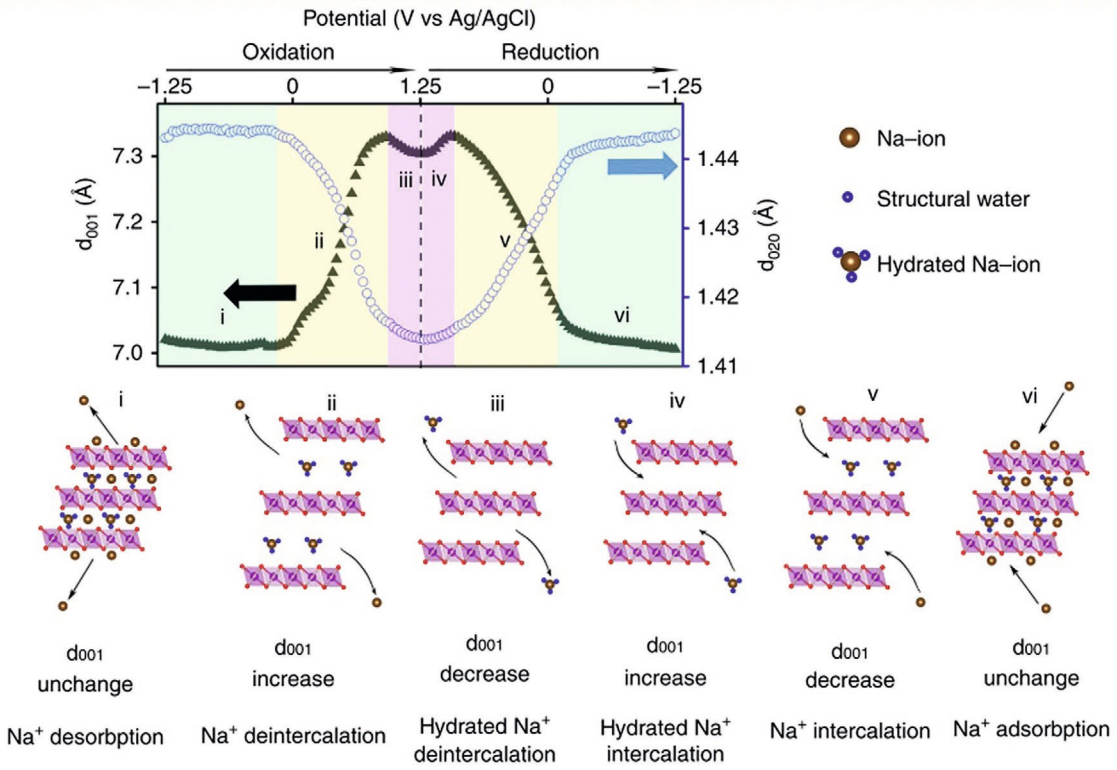

Figure 13. Schematic of Na-ion and water motion during the redox processes, which shows co-deintercalation/coinsertion of Na^+ ions and water within the interlayer region of the $Na_{0.27}MnO_2$ during charging/ discharging processes. Reproduced under the terms of the CC-BY Creative Commons Attribution 4.0 International license (https://creativecommons.org/licenses/by/4.0).[146] Copyright 2019, The Authors, published by Springer Nature.

Li^+ ions for δ-MnO_2; iv) the preintercalated ions can expand the interlayer spacing to enhance structural stability due to the decreased electrostatic and physical interaction between the inserted Zn^{2+} and [MnO_6] layers; v) sole preintercalating crystal water cannot well depress the phase transformation of MnO_2 materials. Besides, in some cases, the coinsertion of ions and coordinated water is a necessary condition to enhance the structural stability of MnO_2 materials.

7. Summary and Prospects

As a promising optimization strategy, preintercalation has been a research hotspot as an issues-oriented solution to overcome several obstacles of MnO_2-based cathode materials, including the low conductivity, low utilization of reversible discharge depth, sluggish diffusion kinetics, and poor structural stability upon cycling. Previous reported preintercalated MnO_2 cathodes have shown dramatic improvements in electrochemical properties, i.e., capacity, rate property, and cycling stability, comparing with the corresponding pristine MnO_2 materials. However, although prior reports have identified many successful cases, challenges and opportunities still exist in practical application of preintercalation strategy.

First, for MnO_2 materials with high amount of preintercalated ions, the electrostatic repulsion between the preintercalated ions and the inserted carrier ions can impede the diffusion of carrier ions, resulting in decreased capacity and rate performance of MnO_2. Thus, the optimum amount and species of preintercalated ions should be carefully screened and tuned to achieve a comprehensive balance of capacity, rate performance, and cycling stability of preintercalated MnO_2 cathodes.

Second, this preintercalation strategy is also applicable to optimize the electrochemical properties of other cathode materials, such as transition metal oxides, sulfides, phosphates, etc., which have tunnel or interlayer spaces for preintercalating the ions/molecules. For instance, this preintercalation strategy can well solve the structural instability and V dissolution issues of vanadate materials, and thus greatly promotes the development of high-performance V-based cathode materials. Therefore, the preintercalation strategy can be a general strategy for optimizing electrochemical properties of cathode materials in various battery applications.

Third, in some preintercalated MnO_2 cathodes, it is inevitable that the preintercalated ions/molecules are extracted from the host structure into the electrolyte during cycling. This process severely removes the advantage of preintercalation strategy. Without the preintercalated ions/molecules, the continuous insertion/extraction of carrier ions caused the structural instability of MnO_2 cathode, and then capacity fading occurs. To inhibit the extraction of the preintercalated ions/ molecules, the preintercalated guest species should be among the monovalent ions (i.e., Rb^+, Cs^+, TMA^+, etc.), multivalent ions (i.e., Zn^{2+}, Ca^{2+}, Ba^{2+}, Al^{3+}, In^{3+}, etc.), and the molecules/polymers with larger molecular weight. Besides, to preintercalate these guest species successfully into the tunnels/interlayers of MnO_2, while taking advantage of existing

preintercalation approaches, more advanced and creative preintercalation approaches need to be developed.

Fourth, despite the enhanced electrochemical performance, the additional cost of the preintercalation strategy must be considered in practical applications. Actually, some preintercalation approaches are too complex and expensive to be used in large-scale industrial production. For instance, it is difficult to realize large-scale industrial preparation of MnO_2 cathodes by approaches of ion-exchange reaction, aqueous/organic interfacial synthesis, and electrochemical reactions with current industrial techniques. Thus, the feasibility of preintercalation approaches must be considerably assessed before practical production of preintercalated MnO_2 materials, and developing simple and general preintercalation approaches for large-scale production is very meaningful.

It has no doubt that the preintercalation strategy is an efficient, and issues-oriented solution to provide a fundamental optimization on electrochemical properties of MnO_2-based materials in various battery applications. A rich variety of preintercalation approaches, and multiple guest species can be tuned and adapted to improve the electrochemical performance of MnO_2. We believe that this review and perspective will provide theoretical insight and offer new ideas for researchers in developing high-performance cathode materials for next-generation batteries.

Supporting Information

Supporting Information is available from the Wiley Online Library or from the author.

Acknowledgements

Q.Z., A.S., and S.D. contributed equally to this work. This work was financially supported by the National Key R&D Program of China (2016YFB0700600) and the Basic and Applied Basic Research Foundation of Guangdong Province (No. 2019A1515110094).

Conflict of Interest

The authors declare no conflict of interest.

Keywords

battery, crystal structure, manganese oxide, preintercalation strategy

Received: April 9, 2020
Revised: July 13, 2020
Published online: November 9, 2020

[1] L. Y. Yang, K. Yang, J. X. Zheng, K. Xu, K. Amine, F. Pan, *Chem. Soc. Rev.* **2020**, *49*, 4667.
[2] J. Lu, Z. Chen, Z. Ma, F. Pan, L. Curtiss, K. Amine, *Nat. Nanotechnol.* **2016**, *11*, 1031.
[3] J. Zheng, J. Lu, K. Amine, F. Pan, *Nano Energy* **2017**, *33*, 497.
[4] J. Liu, Q. Zhao, L. Yang, Y. Lin, F. Pan, *Chin. J. Struct. Chem.* **2020**, *39*, 395.
[5] T. Xiong, Z. Yu, H. Wu, Y. Du, Q. Xie, J. Chen, Y. Zhang, S. Pennycook, W. Lee, J. Xue, *Adv. Energy Mater.* **2019**, *9*, 1803815.
[6] J. Zheng, W. Deng, Z. Hu, Z. Zhuo, F. Liu, H. Chen, Y. Lin, W. Yang, K. Amine, R. Li, J. Lu, F. Pan, *ACS Energy Lett.* **2018**, *3*, 65.
[7] J. Zheng, Y. Ye, T. Liu, Y. Xiao, C. Wang, F. Wang, F. Pan, *Acc. Chem. Res.* **2019**, *52*, 2201.
[8] T. Liu, A. Dai, J. Lu, Y. Yuan, Y. Xiao, L. Yu, M. Li, J. Gim, L. Ma, J. Liu, C. Zhan, L. Li, J. Zheng, Y. Ren, T. Wu, R. Shahbazian-Yassar, J. Wen, F. Pan, K. Amine, *Nat. Commun.* **2019**, *10*, 4721.
[9] G. Yadav, J. Gallaway, D. Turney, M. Nyce, J. Huang, X. Wei, S. Banerjee, *Nat. Commun.* **2017**, *8*, 14424.
[10] M. M. Thackeray, *Prog. Solid State Chem.* **1997**, *25*, 1.
[11] Z. Yin, T. Li, L. Huang, F. Pan, S. Sun, *Chin. J. Struct. Chem.* **2020**, *39*, 20.
[12] Y. Wang, J. Liu, B. Lee, R. Qiao, Z. Yang, S. Xu, X. Yu, L. Gu, Y. Hu, W. Yang, K. Kang, H. Li, X. Yang, L. Chen, X. Huang, *Nat. Commun.* **2015**, *6*, 6401.
[13] X. Sun, V. Duffort, B. L. Mehdi, N. D. Browning, L. F. Nazar, *Chem. Mater.* **2016**, *28*, 534.
[14] R. Zhang, X. Yu, K. Nam, C. Ling, T. Arthur, W. Song, A. Knapp, S. Ehrlich, X. Yang, M. Matsui, *Electrochem. Commun.* **2012**, *23*, 110.
[15] M. Liu, Q. Zhao, H. Liu, J. Yang, X. Chen, L. Yang, Y. Cui, W. Huang, W. Zhao, A. Song, Y. Wang, S. Ding, Y. Song, G. Qian, H. Chen, F. Pan, *Nano Energy* **2019**, *64*, 103942.
[16] Q. Zhao, X. Chen, Z. Wang, L. Yang, R. Qin, J. Yang, Y. Song, S. Ding, M. Weng, W. Huang, J. Liu, W. Zhao, G. Qian, K. Yang, Y. Cui, H. Chen, F. Pan, *Small* **2019**, *15*, 1904545.
[17] Q. Zhao, S. Ding, A. Song, R. Qin, F. Pan, *Chin. J. Struct. Chem.* **2020**, *39*, 388.
[18] A. Boisset, L. Athouël, J. Jacquemin, P. Porion, M. Anouti, *J. Phys. Chem. C* **2013**, *117*, 7408.
[19] B. Byles, N. Palapati, A. Subramanian, E. Pomerantseva, *APL Mater.* **2016**, *4*, 046108.
[20] R. Inoue, M. Ryota, *ECS Trans.* **2010**, *25*, 71.
[21] M. Alfaruqi, S. Islam, V. Mathew, J. Song, S. Kim, D. Tung, J. Jo, S. Kim, J. Baboo, Z. Xiu, *Appl. Surf. Sci.* **2017**, *404*, 435.
[22] Y. Yuan, C. Zhan, K. He, H. Chen, W. Yao, S. Sharifiasl, B. Song, Z. Yang, A. Nie, X. Luo, *Nat. Commun.* **2016**, *7*, 13374.
[23] G. Liu, H. Huang, R. Bi, X. Xiao, T. Ma, L. Zhang, *J. Mater. Chem. A* **2019**, *7*, 20806.
[24] J. Huang, Z. Wang, M. Hou, X. Dong, Y. Liu, Y. Wang, Y. Xia, *Nat. Commun.* **2018**, *9*, 2906.
[25] H. Zhang, Q. Liu, J. Wang, K. Chen, D. Xue, J. Liu, X. Lu, *J. Mater. Chem. A* **2019**, *7*, 22079.
[26] K. Lu, Z. Hu, Z. Xiang, J. Ma, B. Song, J. Zhang, H. Ma, *Angew. Chem., Int. Ed.* **2016**, *55*, 10448.
[27] D. Chao, W. Zhou, C. Ye, Q. Zhang, Y. Chen, L. Gu, K. Davey, S. Qiao, *Angew. Chem., Int. Ed.* **2019**, *58*, 7823.
[28] P. Yu, Y. Zeng, H. Zhang, M. Yu, Y. Tong, X. Lu, *Small* **2019**, *15*, 1804760.
[29] X. Zeng, J. Hao, Z. Wang, J. Mao, Z. Guo, *Energy Storage Mater.* **2019**, *20*, 410.
[30] W. Li, C. Hang, Y. Wang, H. Liu, *Chin. J. Struct. Chem.* **2020**, *39*, 31.
[31] B. Lee, C. Yoon, H. Lee, K. Chung, B. Cho, S. Oh, *Sci. Rep.* **2015**, *4*, 6066.
[32] B. Lee, H. Lee, H. Kim, K. Chung, B. Cho, S. Oh, *Chem. Commun.* **2015**, *51*, 9265.
[33] H. Shi, X. Sun, *Chem* **2020**, *6*, 817.
[34] J. Kim, D. Kim, D. Oh, H. Lee, J. Lee, Y. Jung, *J. Power Sources* **2015**, *274*, 1254.
[35] J. Lu, C. Zhan, T. Wu, J. Wen, Y. Lei, A. J. Kropf, H. Wu, D. Miller, J. Elam, Y. Sun, *Nat. Commun.* **2014**, *5*, 5693.
[36] X. Yao, Y. Zhao, F. Castro, L. Mai, *ACS Energy Lett.* **2019**, *4*, 771.
[37] F. Wan, Y. Zhang, L. Zhang, D. Liu, C. Wang, L. Song, Z. Niu, J. Chen, *Angew. Chem., Int. Ed.* **2019**, *58*, 7062.

[38] Y. Zhao, C. Han, J. Yang, J. Su, X. Xu, S. Li, L. Xu, R. Fang, H. Jiang, X. Zou, B. Song, L. Mai, Q. Zhang, *Nano Lett.* **2015**, *15*, 2180.
[39] G. Fang, J. Zhou, A. Pan, S. Liang, *ACS Energy Lett.* **2018**, *3*, 2480.
[40] M. Song, T. Hua, D. Chao, H. Fan, *Adv. Funct. Mater.* **2018**, *28*, 1802564.
[41] J. Joseph, J. Nerkar, C. Tang, A. Du, A. O'Mullane, K. Ostrikov, *ChemSusChem* **2019**, *12*, 3753.
[42] C. Wei, C. Xu, B. Li, H. Du, D. Nan, F. Kang, *J. Power Sources* **2013**, *225*, 226.
[43] P. Gao, P. Metz, T. Hey, Y. Gong, D. Liu, D. Edwards, J. Howe, R. Huang, S. Misture, *Nat. Commun.* **2017**, *8*, 14559.
[44] Z. Liu, X. Yang, Y. Makita, K. Ooi, *Chem. Mater.* **2002**, *14*, 4800.
[45] M. Wang, S. Yagi, *J. Alloy Compd.* **2020**, *820*, 153135.
[46] Y. Wang, W. Wu, L. Cheng, P. He, C. Wang, Y. Xia, *Adv. Mater.* **2008**, *20*, 2166.
[47] T. Wu, D. Hesp, V. Dhanak, C. Collins, L. Hardwick, C. Hu, *J. Mater. Chem. A* **2015**, *3*, 12786.
[48] K. Kang, G. Ceder, *Phys. Rev. B* **2006**, *74*, 094105.
[49] R. Zhao, L. Zhang, C. Wang, L. Yin, *J. Power Sources* **2017**, *353*, 77.
[50] X. Wang, P. Hu, C. Niu, J. Meng, X. Xu, X. Wei, C. Tang, W. Luo, L. Zhou, Q. An, L. Mai, *Nano Energy* **2017**, *35*, 71.
[51] K. Nam, S. Kim, E. Yang, Y. Jung, E. Levi, D. Aurbach, J. Choi, *Chem. Mater.* **2015**, *27*, 3721.
[52] N. C. Frey, B. Byles, H. Kumar, D. Er, E. Pomerantseva, V. Shenoy, *Phys. Chem. Chem. Phys.* **2018**, *20*, 9480.
[53] Y. Li, S. Wang, J. Salvador, J. Wu, B. Liu, W. Yang, J. Yang, W. Zhang, J. Liu, J. Yang, *Chem. Mater.* **2019**, *31*, 2036.
[54] M. Alfaruqi, S. Islam, D. Putro, V. Mathew, S. Kim, J. Jo, S. Kim, Y. Sun, K. Kim, J. Kim, *Electrochim. Acta* **2018**, *276*, 1.
[55] B. Lin, X. Zhu, L. Fang, X. Liu, S. Li, T. Zhai, L. Xue, Q. Guo, J. Xu, H. Xia, *Adv. Mater.* **2019**, *31*, 1900060.
[56] A. Radhiyah, M. Izwan, V. Baiju, C. Feng, I. Jamil, R. Jose, *RSC Adv.* **2015**, *5*, 9667.
[57] K. Chen, W. Pan, D. Xue, *J. Phys. Chem. C* **2016**, *120*, 20077.
[58] L. Mai, H. Li, Y. Zhao, L. Xu, X. Xu, Y. Luo, Z. Zhang, W. Ke, C. Niu, Q. Zhang, *Sci. Rep.* **2013**, *3*, 1718.
[59] J. Zheng, Y. Ye, F. Pan, *Natl. Sci. Rev.* **2020**, *7*, 242.
[60] M. Young, A. Holder, S. George, C. Musgrave, *Chem. Mater.* **2015**, *27*, 1172.
[61] K. Zhang, X. Han, Z. Hu, X. Zhang, Z. Tao, J. Chen, *Chem. Soc. Rev.* **2015**, *44*, 699.
[62] O. Ghodbane, J. Pascal, F. Favier, *ACS Appl. Mater. Interfaces* **2009**, *1*, 1130.
[63] B. Pinaud, Z. Chen, D. Abram, T. Jaramillo, *J. Phys. Chem. C.* **2011**, *115*, 11830.
[64] Q. Ye, R. Dong, Z. Xia, G. Chen, H. Wang, G. Tan, L. Jiang, F. Wang, *Electrochim. Acta* **2014**, *141*, 286.
[65] H. Xia, X. Zhu, J. Liu, Q. Liu, S. Lan, Q. Zhang, X. Liu, J. Seo, T. Chen, L. Gu, Y. Meng, *Nat. Commun.* **2018**, *9*, 5100.
[66] Z. Hu, X. Xiao, L. Huang, C. Chen, T. Li, T. Su, X. Cheng, L. Miao, Y. Zhang, J. Zhou, *Nanoscale* **2015**, *7*, 16094.
[67] A. Poyraz, J. Huang, C. Pelliccione, X. Tong, S. Cheng, A. Marschilok, K. Takeuchi, E. Takeuchi, *J. Mater. Chem. A* **2017**, *5*, 16914.
[68] K. Sada, B. Senthilkumar, P. Barpanda, *J. Mater. Chem. A* **2019**, *7*, 23981.
[69] Y. Li, A. Poyraz, X. Hu, M. Cuiffo, C. Clayton, L. Wu, Y. Zhu, E. Takeuchi, A. Marschilok, K. Takeuchi, *J. Electrochem. Soc.* **2017**, *164*, A2151.
[70] A. Radhamani, M. Surendra, M. Rao, *Appl. Surf. Sci.* **2018**, *450*, 209.
[71] W. Xu, J. Wan, W. Huo, Q. Yang, Y. Li, C. Zhang, X. Gu, C. Hu, *Chem. Eng. J.* **2018**, *354*, 1050.
[72] J. Kang, A. Hirata, L. Kang, X. Zhang, Y. Hou, L. Chen, C. Li, T. Fujita, K. Akagi, M. Chen, *Angew. Chem., Int. Ed.* **2013**, *52*, 1664.
[73] H. Zhang, K. Ye, X. Huang, X. Wang, K. Cheng, X. Xiao, G. Wang, D. Cao, *J. Power Sources* **2017**, *338*, 136.
[74] L. Peng, Y. Zhu, X. Peng, Z. Fang, W. Chu, Y. Wang, Y. Xie, Y. Li, J. J. Cha, G. Yu, *Nano Lett.* **2017**, *17*, 6273.
[75] V. Augustyn, P. Simon, B. Dunn, *Energy Environ. Sci.* **2014**, *7*, 1597.
[76] S. Wen, J. Lee, I. Yeo, J. Park, S. Mho, *Electrochim. Acta* **2004**, *50*, 849.
[77] J. Kim, V. Augustyn, B. Dunn, *Adv. Energy Mater.* **2012**, *2*, 141.
[78] V. Augustyn, J. Come, M. Lowe, J. Kim, P. Taberna, S. Tolbert, H. Abruña, P. Simon, B. Dunn, *Nat. Mater.* **2013**, *12*, 518.
[79] Y. Zhang, Y. An, J. Jiang, S. Dong, L. Wu, R. Fu, H. Dou, X. Zhang, *Energy Technol.* **2018**, *6*, 2146.
[80] Z. Sun, Y. Zhen, Y. Liu, J. Fu, S. Cheng, P. Cui, E. Xie, *J. Power Sources* **2019**, *436*, 226795.
[81] N. Jabeen, Q. Xia, S. Savilov, S. Aldoshin, Y. Yu, H. Xia, *ACS Appl. Mater. Interfaces* **2016**, *8*, 33732.
[82] S. Lin, Y. Lu, J. Wang, C. Ma, C. Hu, *J. Power Sources* **2018**, *400*, 415.
[83] S. Lin, Y. Lu, Y. Chien, J. Wang, P. Chen, C. Ma, C. Hu, *J. Power Sources* **2018**, *393*, 1.
[84] P. Chen, A. Adomkevicius, Y. Lu, S. Lin, Y. Tu, C. Hu, *J. Electrochem. Soc.* **2019**, *166*, A1875.
[85] Q. Zhang, M. Levi, Q. Dou, Y. Lu, Y. Chai, S. Lei, H. Ji, B. Liu, X. Bu, *Adv. Energy Mater.* **2019**, *9*, 1802707.
[86] P. Shearing, Z. Li, S. Gadipelli, H. Li, C. Howard, Z. Guo, I. Parkin, F. Li, *Nat. Energy* **2020**, *5*, 160.
[87] J. Zheng, Y. Wei, S. Cui, X. Song, Y. Su, W. Deng, Z. Wu, X. Wang, W. Wang, M. Rao, Y. Lin, C. Wang, K. Amine, F. Pan, *J. Am. Chem. Soc.* **2015**, *137*, 8364.
[88] P. He, M. Yan, Y. Chen, S. Wang, Q. Wei, K. Zhao, X. Xu, Q. An, Y. Shuang, Y. Shao, K. Mueller, L. Mai, J. Liu, J. Yang, *Adv. Mater.* **2018**, *30*, 1703725.
[89] A. Poyraz, J. Huang, S. Cheng, L. Wu, X. Tong, Y. Zhu, A. Marschilok, K. Takeuchi, E. Takeuchi, *J. Electrochem. Soc.* **2017**, *164*, A1983.
[90] J. Jo, J. Hwang, J. Choi, S. Myung, *ACS Appl. Mater. Interfaces* **2019**, *11*, 43312.
[91] E. Levi, Y. Gofer, D. Aurbach, *Chem. Mater.* **2010**, *22*, 860.
[92] H. D. Yoo, I. Shterenberg, Y. Gofer, G. Gershinsky, N. Pour, D. Aurbach, *Energy Environ. Sci.* **2013**, *6*, 2265.
[93] X. Deng, Y. Xu, Q. An, F. Xiong, S. Tan, L. Wu, L. Mai, *J. Mater. Chem. A* **2019**, *7*, 10644.
[94] Y. Xu, X. Deng, Q. Li, G. Zhang, F. Xiong, S. Tan, Q. Wei, J. Lu, J. Li, Q. An, L. Mai, *Chem* **2019**, *5*, 1194.
[95] C. Wei, C. Xu, B. Li, H. Du, F. Kang, *J. Phys. Chem. Solids* **2012**, *73*, 1487.
[96] J. Song, M. Noked, E. Gillette, J. Duay, G. Rubloff, S. Lee, *Phys. Chem. Chem. Phys.* **2015**, *17*, 5256.
[97] C. Yuan, Y. Zhang, Y. Pan, X. Liu, G. Wang, D. Cao, *Electrochim. Acta* **2014**, *116*, 404.
[98] K. Nam, S. Kim, S. Lee, M. Salama, I. Shterenberg, Y. Gofer, J.-S. Kim, E. Yang, C. S. Park, J.-S. Kim, S.-S. Lee, W.-S. Chang, S.-G. Doo, Y. N. Jo, Y. Jung, D. Aurbach, J. W. Choi, *Nano Lett.* **2015**, *15*, 4071.
[99] K. Nam, H. Kim, J. Choi, J. Choi, *Energy Environ. Sci.* **2019**, *12*, 1999.
[100] D. Kundu, B. Adams, V. Duffort, S. Vajargah, L. Nazar, *Nat. Energy* **2016**, *1*, 16119.
[101] N. Li, C. L. Ma, B. Dong, D. Fang, Z. Liu, Y. Zhao, X. Li, J. Fan, S. Chen, S. Zhang, C. Zhi, *Adv. Funct. Mater.* **2019**, *29*, 1906142.
[102] N. Zhang, Y. Dong, M. Jia, X. Bian, Y. Wang, M. Qiu, J. Xu, Y. Liu, L. Jiao, F. Cheng, *ACS Energy Lett.* **2018**, *3*, 1366.
[103] J. Lee, J. Ju, W. Cho, B. Cho, S. Oh, *Electrochim. Acta* **2013**, *112*, 138.
[104] H. Liu, C. Guo, J. Li, Z. Hou, J. Liang, J. Zhou, Y. Zhu, Y. Qian, *Electrochim. Acta* **2019**, *304*, 405.
[105] N. Kumagai, T. Sasaki, S. Oshitari, S. Komaba, *J. New Mater. Electrochem. Syst.* **2006**, *9*, 175.
[106] Y. Yang, D. Shu, J. K. You, Z. Lin, *J. Power Sources* **1999**, *81–82*, 637.
[107] Y. Li, S. Cui, Q. Shi, L. Mi, W. Chen, *CrystEngComm* **2016**, *18*, 3136.
[108] L. Cao, B. Yu, T. Cheng, X. Zheng, X. Li, W. Li, Z. Ren, H. Fan, *Ceram. Int.* **2017**, *43*, 14897.

[109] M. Nakayama, S. Konishi, H. Tagashira, K. Ogura, *Langmuir* **2005**, *21*, 354.
[110] Y. Zhang, S. Deng, G. Pan, H. Zhang, B. Liu, X. Wang, J. Tu, *Small Methods* **2020**, *4*, 1900828.
[111] J. Kim, K. Kim, W. Cho, W. Shin, R. Kanno, J. Choi, *Nano Lett.* **2012**, *12*, 6358.
[112] W. Pang, V. Peterson, N. Sharma, C. Zhang, Z. Guo, *J. Phys. Chem. C* **2014**, *118*, 3976.
[113] Y. Yuan, A. Nie, G. Odegard, R. Xu, D. Zhou, S. Santhanagopalan, K. He, H. Asayesh-Ardakani, D. Meng, R. Klie, C. Johnson, J. Lu, R. Shahbazian-Yassar, *Nano Lett.* **2015**, *15*, 2998.
[114] Y. Mizuno, M. Okubo, E. Hosono, T. Kudo, H. Zhou, K. Oh-ishi, *J. Phys. Chem. C* **2013**, *117*, 10877.
[115] M. Alfaruqi, S. Kim, J. Song, D. Pham, J. Jo, Z. Xiu, V. Mathew, J. Kim, *Electrochem. Commun.* **2015**, *60*, 121.
[116] B. Hertzberg, J. Gallaway, Z. Zhong, M. Croft, D. Turney, G. Yadav, D. Steingart, C. Erdonmez, S. Banerjee, *J. Power Sources* **2016**, *321*, 135.
[117] S. Donne, M. Bailey, *J. Electrochem. Soc.* **2012**, *159*, A2010.
[118] I. Kottegoda, S. Kobayashi, Y. Uchimoto, M. Wakihara, *J. Mater. Chem.* **2004**, *14*, 1843.
[119] K. Goransson, H. Berg, B. NolaÈng, J. Thomas, *J. Mater. Chem.* **1999**, *9*, 2813.
[120] R. Shannon, *Acta Crystallogr.* **1976**, *32*, 751.
[121] X. Lia, Y. Xu, C. Wang, *J. Alloys Compd.* **2009**, *479*, 310.
[122] Y. Shin, D. Jang, S. Oh, *J. Electrochem. Soc.* **1996**, *143*, 1562.
[123] M. Suzuki, K. Kim, S. Taminato, K. Tamura, J. Son, J. Mizuki, R. Kanno, *J. Electrochem. Soc.* **2015**, *162*, A7083.
[124] T. Ma, H. Chen, F. Zhu, Y. Zeng, X. Qiu, X. Guo, *Int. J. Electrochem. Sci.* **2017**, *12*, 7817.
[125] M. Jayakumar, K. Hemalatha, P. Berac, A. Prakash, *J. Mater. Chem. A* **2015**, *3*, 20908.
[126] X. Sun, J. Wang, H. Zhao, L. Xu, J. Xia, M. Luo, *J. Phys. Chem. C* **2019**, *123*, 22735.
[127] Y. Shao, H. Pan, P. Yan, Y. Cheng, K. Han, Z. Nie, C. Wang, J. Yang, X. Li, P. Bhattachary, K. Mueller, J. Liu, *Nat. Energy* **2016**, *1*, 16039.
[128] G. Fang, C. Zhu, M. Chen, J. Zhou, B. Tang, X. Cao, S. Liang, *Adv. Funct. Mater.* **2019**, *29*, 1808375.
[129] D. Ahn, I. Yoo, Y. Koo, N. Shin, J. Kim, *J. Mater. Chem.* **2011**, *21*, 5282.
[130] L. Yu. J. Liu, E. Hu, B. Guiton, X. Yang, K. Page, *Inorg. Chem.* **2018**, *57*, 6873.
[131] K. Aldi, J. Cabana, P. Sideris, C. Grey, *Am. Mineral.* **2012**, *97*, 883.
[132] V. Muhammad, H. Alfaruqi, J. Gim, J. Baboo, S. Choi, J. Kim, *Chem. Mater.* **2015**, *27*, 3609.
[133] S. Islam, V. Mathew, J. Song, S. Kim, S. Kim, J. Jo, J. Baboo, D. Pham, D. Putro, Y. Sunb, J. Kim, *J. Mater. Chem. A* **2017**, *5*, 23299.
[134] J. Hao, J. Zhang, L. Dong, W. Liu, C. Xu, F. Kang, *Electrochim. Acta* **2018**, *259*, 170.
[135] X. Li, D. Su, L. Liu, R. Chisnell, S. Ong, H. Chen, A. Toumar, J. Idrobo, Y. Lei, J. Bai, F. Wang, J. Lynn, Y. Lee, G. Ceder, *Nat. Mater.* **2014**, *13*, 586.
[136] J. Seo, H. Chung, P. Meng, X. Wang, Y. Meng, *J. Phys. Chem. C* **2018**, *122*, 11177.
[137] J. Huang, A. Poyraz, S. Lee, L. Wu, Y. Zhu, A. Marschilok, K. Takeuchi, E. Takeuchi, *ACS Appl. Mater. Interfaces* **2017**, *9*, 4333.
[138] M. Alfaruqi, S. Kim, J. Song, V. Mathew, J. Kim, *J. Power Sources* **2015**, *288*, 320.
[139] B. Wu, G. Zhang, M. Yan, T. Xiong, P. He, L. He, X. Xu, L. Mai, *Small* **2018**, *14*, 1703850.
[140] C. Ling, T. Arthura, F. Mizuno, *Chem. Mater.* **2015**, *27*, 1507271.
[141] J. Lim, Y. Lim, M. Park, Y. Kim, M. Cho, K. Cho, *J. Mater. Chem. A* **2015**, *3*, 7066.
[142] Y. Qiao, Y. Liu, W. Zhang, H. Xu, L. Yuan, X. Hu, X. Dai, Y. Huang, *Nano Energy* **2014**, *5*, 97.
[143] X. Shan, D. Charles, Y. Lei, R. Qiao, G. Wang, W. Yang, M. Feygenson, D. Su, X. Teng, *Nat. Commun.* **2016**, *7*, 13370.
[144] X. Zhu, H. Xia, J. Liu, Q. Liu, S. Lan, Q. Zhang, X. Liu, J. Seo, T. Chen, L. Gu, Y. Meng, *Nat. Commun.* **2018**, *9*, 5100.
[145] Y. Kim, M. Jo, J. Yang, M. Jeong, K. Song, Y. Kim, J. Lim, M. Cho, J. Shim, Y. Kim, W. Yoon, Y. Kang, *Nat. Commun.* **2019**, *10*, 3385.
[146] F. Guo, X. Shan, D. Charles, Z. Lebens-Higgins, W. Yang, S. Razek, L. Piper, X. Teng, *Nat. Commun.* **2019**, *10*, 4975.
[147] S. Han, D. Li, V. Petkov, P. Phillips, H. Wang, J. Kim, K. More, B. Key, R. Klie, T. Fister, N. Markovic, A. Burrell, S. Tepavcevic, J. Vaughey, *Chem. Mater.* **2017**, *29*, 4874.
[148] B. Han, S. Zhao, D. Zhang, Q. Huang, Y. Deng, W. Wei, *J. Mater. Chem. A* **2018**, *6*, 5733.
[149] J. Hyoung, J. Heo, S. Hong, *J. Power Sources* **2018**, *390*, 127.
[150] C. Johnson, *J. Power Sources* **2007**, *165*, 559.
[151] J. Huang, K. Takeuchi, E. Takeuchi, A. Marschilok, *Chem. Commun.* **2016**, *52*, 4088.
[152] J. Liu, J. Cai, S. Suib, M. Aindow, *J. Phys. Chem. B* **2003**, *107*, 9185.
[153] M. Thackeray, C. Johnson, *J. Power Sources* **2001**, *97*, 437.
[154] B. Li, D. Zhai, C. Xu, H. Du, C. Wei, F. Kang, *J. Power Sources* **2011**, *196*, 7860.
[155] H. Jang, S. Suzuki, M. Miyayama, *J. Eur. Ceram. Soc.* **2014**, *34*, 4297.
[156] J. Wang, J. Wang, H. Liu, C. Wei, F. Kang, *J. Mater. Chem. A* **2019**, *7*, 13727.

Qinghe Zhao received his B.S. degree from the University of Science and Technology of Beijing (USTB), China in 2010, and earned his Ph.D. degree from the School of Advanced Materials at USTB in 2016, majoring in the electrochemical corrosion behavior of iron-based alloys, under the supervision of Prof. Minxu Lu. He is now an associate researcher in the School of Advanced Materials, Peking University Shenzhen Graduate School, China. His research interests mainly focus on the key materials and technologies for energy storage and conversion applications, including electrocatalysts and zinc-ion and sodium-ion batteries

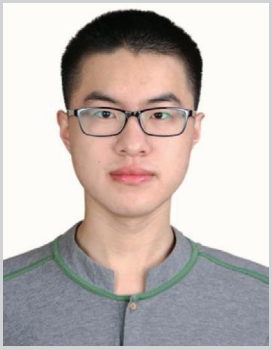

Aoye Song graduated with a B.S. degree from the College of Chemistry and Molecular Engineering of Peking University (PKU), China in 2018. During his undergraduate studies, he majored in the modification of NMC-material lithium-ion batteries under the guidance of Prof. Heng-hui Zhou. He is now pursuing a master's degree with Prof. Feng Pan in the School of Advanced Materials, Peking University Shenzhen Graduate School, China. His main research interests are advanced energy-storage materials, especially in the areas of zinc-ion aqueous batteries.

Shouxiang Ding graduated from South China University of Technology (SUCT) China, receiving his B.S. degree from the School of Chemistry and Chemical Engineering in 2019. He is currently a postgraduate student in Prof. Feng Pan' s group in the School of Advanced Materials, Peking University Shenzhen Graduate School. His research interests focus on developing cathode materials for aqueous zinc-ion batteries.

Runzhi Qin received his B.S. degree from the University of Science and Technology of Beijing (USTB), China in 2013, and earned his Ph.D. degree from the School of Materials Science and Technology at USTB in 2019, majoring in the electrochemical corrosion behavior of iron-based alloys, under the supervision of Prof. Minxu Lu. He now holds a post-doctoral position in Prof. Feng Pan's group in the School of Advanced Materials, Peking University Shenzhen Graduate School, China. His research interests mainly focus on the key materials and technologies for zinc-based batteries.

Yanhui Cui received his B.E. degree in packing engineering from Zhengzhou University, China, in 2010. Following this, he completed his Master's and Ph.D. degrees under the supervision of Prof. Andrew Baker and Junwei Wu in materials science at Harbin Institute of Technology (Shenzhen) in 2014 and 2018, respectively. He is now a postdoctoral researcher in the School of Advanced Materials, Peking University Shenzhen Graduate School (China), in Prof. Feng Pan's group. His research interests focus on the fields of energy storage and conversion.

Shunning Li received his B.E. degree in 2013 and Ph.D. degree in 2018 from the School of Materials Science and Engineering, Tsinghua University, China. Currently, he is a postdoc in the group of Prof. Feng Pan in the School of Advanced Materials at Peking University, Shenzhen Graduate School, China. His research interests focus on the first-principles design of energy storage materials and heterogeneous catalysts.

Feng Pan, chair-professor, founding dean of the School of Advanced Materials, Peking University, Shenzhen Graduate School, director of National Center of Electric Vehicle Power Battery and Materials for International Research, received his B.S. degree from the Department of Chemistry, Peking University in 1985 and his Ph.D. from the Department of P&A Chemistry, University of Strathclyde, UK. He has been engaged in fundamental research on structural chemistry, exploring the "Material Gene" for Li-ion batteries, and developing novel energy conversion–storage materials and devices.